Chapter 7
Design and Principles of Linear Accelerators and Colliders

J. Seeman, D. Schulte, J. P. Delahaye, M. Ross, S. Stapnes, A. Grudiev, A. Yamamoto, A. Latina, A. Seryi, R. Tomás García, S. Guiducci, Y. Papaphilippou, S. A. Bogacz, and G. A. Krafft

7.1 General Introduction on Linear Accelerators

J. Seeman

Linear accelerators (linacs) use alternating radiofrequency (RF) electromagnetic fields to accelerate charged particles in a straight line. Linacs were invented about 95 years ago and have seen many significant technical innovations since. A

Coordinated by J. Seeman, J. P. Delahaye.

J. Seeman · M. Ross
SLAC National Accelerator Laboratory, Stanford University, Menlo Park, CA, USA
e-mail: seeman@slac.stanford.edu; mcrec@slac.stanford.edu

D. Schulte · J. P. Delahaye (✉) · S. Stapnes · A. Grudiev · A. Latina · R. Tomás García · Y. Papaphilippou
CERN (European Organization for Nuclear Research) Meyrin, Geneva, Switzerland
e-mail: daniel.schulte@cern.ch; Jean-Pierre.Delahaye@cern.ch; steinar.stapnes@cern.ch; alexej.grudiev@cern.ch; andrea.latina@cern.ch; rogelio.tomas@cern.ch; ioannis.papaphilippou@cern.ch

A. Yamamoto
KEK, Tsukuba, Ibaraki, Japan

CERN (European Organization for Nuclear Research) Meyrin, Geneva, Switzerland
e-mail: akira.yamamoto@cern.ch

A. Seryi · S. A. Bogacz · G. A. Krafft
Center for Advanced Studies of Accelerators, Jefferson Lab, Newport News, VA, USA
e-mail: seryi@jlab.org; bogacz@jlab.org; krafft@jlab.org

S. Guiducci
National Laboratory of Frascati/National Institute for Nuclear Physics, Frascati, Roma, Italy
e-mail: susanna.guiducci@lnf.infn.it

S. Myers, H. Schopper (eds.), *Particle Physics Reference Library*,
https://doi.org/10.1007/978-3-030-34245-6_7

wide range of particle beams have been accelerated with linacs including beams of electrons, positrons, protons, antiprotons, and heavy ions. Linac parameter possibilities include pulsed versus continuous wave, low and high beam powers, low and high repetition rates, low transverse emittance beams, short bunches with small energy spreads, and accelerated multiple bunches in a single pulse. The number of linacs around the world has grown tremendously with thousands of linacs in present use, many for medical therapy, in industry, and for research and development in a broad spectrum of scientific fields. Researchers have developed accelerators for scientific tools in their own right, being awarded several Nobel prizes. Moreover, linacs and particle accelerators in general have enabled many discovery level science experiments in related fields, resulting in many Nobel prizes as well.

In this chapter the various types, near term uses, and future directions of linacs are discussed. There are many standard types of linac structures, several are shown in Figs. 7.1 and in Figs. 7.6 and 7.7 in Sect. 7.4. A complete linac system includes an RF power source, the microwave power waveguide distribution, the accelerating structure itself, a power load, a control system, a vacuum system, survey-alignment, a cooling system, and beam diagnostics such as beam position monitors and profile monitors. Examples of present operating linacs from around the world, linacs under construction, and proposed large scale linacs are shown in Table 7.1 [3–11]. There are many constraints to design a successful linac [12, 13] with the basic being to

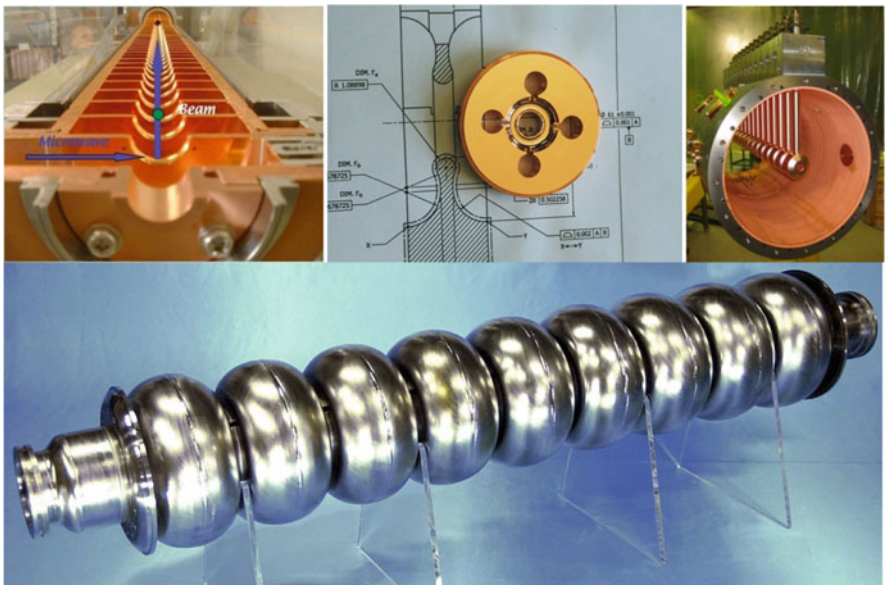

Fig. 7.1 Examples of linac structures: Cu linac 3-GHz (upper left), Cu cells 12-GHz (upper centre), Drift Tube Linac 202-MHz (upper right), and Super-conducting 9-cell cavity 1.3-GHz (lower centre)

Table 7.1 Several existing and near future (F) Linacs used for scientific studies in the world

Location	Length (m)	E (GeV)	G (MV/m)	Part.	RF Freq. (MHz)	Type
DAPHNE, IT	60	0.51	17	e−/e+	2856	NC-Cu-constant grad
Linac, KEK	608	8.0	15	e−/e+	2856	NC-Cu-constant grad
SLC/LCLS, SLAC	3000	54.0	18	e−/e+	2856	NC-Cu-constant grad
SwissFEL	620	5.8	28		5712	NC-Cu-constant grad
CLS-II, SLAC (F)	500	4.1	16	e−	1300	SC-CW-9-cell cavities
J-PARC, JP	400	0.18/0.4	2	p	324/972	RFQ/DTL/SDTL/ACS
SNS, ORNL	493	0.97	10	p	402/805	RFQ/DTL/CCL/SC
Spring8FEL, JP	400	8.0	35	e−	5712	NC-Cu-constant imp
E-XFEL, DESY	1700	17.5	23.6	e−	1300	SC-Nb-9-cell cavities
ILC, World (F)	2×11300	250	35	e−/e+	1300	SC-Nb-9-cell cavities
CLIC, World (F)	2×21000	1500	100	e−/e+	12,000	NC-travelling wave

choose an RF structure such that electromagnetic fields and the beam particles are in phase as the beam traverses each cell in the RF cavity. Much of the design work has gone into maximizing the accelerating gradients, avoiding arcing, RF discharges, and multipacting, to minimize the construction costs, and to make efficient use of overall AC power. Proton and ion beams are often made in drift tube linacs (DTL) with gradients of 2–8 MeV/m using RF frequencies of 30–400 MHz. Electron linacs are typically made of either copper structures with 15–75 MeV/m at 3–12 GHz or superconducting structures with 10–30 MeV/m near 1.3 GHz. Small proton or ion linacs are used for medical therapy and patient diagnostics. Larger proton linacs are injectors for large particle colliders or proton drivers for neutron or neutrino production. Small electron linacs are used for electron or gamma ray medical therapy and in industry. Large electron linacs are often injectors into GeV energy storage rings for synchrotron radiation sources and e−/e+ colliders and as injectors into FEL undulators.

An active area of present research is the conditioning of beams in linacs to make them useful for high energy physics, basic energy sciences, nuclear physics, material sciences, and technology security. These beam parameters include the calculation and control of longitudinal and transverse wakefields (Sect. 7.5), low emittance generation and preservation (Sect. 7.7), incoherent and coherent synchrotron radiation effects, electron cloud effects, ion effects, energy recovery through recirculation (Sect. 7.8), multibunch effects (Sect. 7.3), high luminosity requirements (Sect. 7.2), final focus systems (Sect. 7.5), 2D and 3D emittance exchanges, and beam-undulator interactions in x-ray FELs.

The use of linacs in energy frontier e+e− colliders is essential to avoid excessive synchrotron radiation in ultrahigh energy beams. The first linear collider used the SLAC linac called the SLC (Sect. 7.2) which provided frontier particle physics results as well as establishing a basis to build upon for a future linear collider design. Recent linear collider studies (Sect. 7.3) have concentrated on the ILC (1.3 GHz Superconducting) [4] and CLIC (12 GHz normal conducting) [7]. Years of studies and experiments have illustrated the approaching viability of these two collider technologies.

Very attractive schemes like for example the energy recovery linacs [14] as described in Sect. 7.8 are being developed. Recent avenues of study for far future linacs are in the area of excited plasmas and dielectrics as structures [15, 16]. Examples are electron beam driven plasma, wakefield accelerator PWFA that recently produced 40 GeV/m acceleration for electrons and 0.23 GeV/m for positrons [17–20] and laser driven plasma wakefield accelerator demonstrating up to 4.2 GeV in a 9 cm plasma [21, 22] as described in Chap. 12. Another active research area is direct laser driven accelerating nanostructures in silicon [23, 24]. New ongoing studies in these technologies will illuminate possible future uses.

7.2 High Luminosity Issues and Beam-Beam Effects

D. Schulte

In linear colliders, the colliding beams have extremely small transverse dimensions $\sigma_{x,y}$ to reach high luminosity. Each beam exerts a strong electro-magnetic force on the other beam, which is focusing in case of electron-positron collisions. This disruption can shrink the beam size significantly during collision, the so-called pinch effect [25–27]. This increases the luminosity but the bending of the particles' trajectories stimulates them to radiate so-called beamstrahlung photons, a process similar to synchrotron radiation [28–32]. Consequently, not all collisions take place at the nominal centre-of-mass energy. Hence, one needs to choose the beam parameters in order to limit the beamstrahlung and to achieve an acceptable luminosity spectrum for the experiment. High luminosity with low beamstrahlung is usually achieved by using flat beams $\sigma_x \gg \sigma_y$) as shown below. Approximate formulae are used, since full analytic treatment of the beam-beam interaction is for most parameters not possible. Simulation codes are used for precise numerical predictions, in particular CAIN and GUINEA-PIG [33–35].

It should be noted that one usually needs a horizontal crossing angle θ_c between the two beam lines at the interaction point. This separation of incoming and outgoing beam allows to efficiently extract collision debris and hence to avoid large beam losses after the collision. For short distances in-between bunches in each beam pulse, the crossing angle also reduces the impact of parasitic crossings of incoming and outgoing bunches. The luminosity reduction due to the crossing angle is avoided by using a so-called crab-crossing scheme. Before the collision a transverse deflecting cavity introduces a rotation around the vertical axis, such that the beams are aligned to the longitudinal axis of the laboratory system at the collision rather than the direction of motion. Hence the two bunches fully overlap during the collision while moving together horizontally, like crabs. In this case the crossing angle hardly affects the beam-beam interaction and can be neglected in the further considerations.

In high energy linear colliders like ILC and CLIC developed in Sect. 7.3, the luminosity is limited by beamstrahlung, the achievable vertical beam size and the efficiency of the main linac RF. This is seen by expressing it as a function of the number of particles per bunch N, the number of bunches per beam pulse n_b, the repetition rate of beam pulses f_r and the luminosity enhancement factor H_D, which tends to be in the range of 1–2:

$$L = H_D \frac{N^2}{4\pi\sigma_x\sigma_y} n_b f_r. \tag{7.1}$$

Ignoring the usually small variations of H_D, one obtains the simple dependence:

$$L \propto \frac{N}{\sigma_x}\frac{1}{\sigma_y}\eta P_{\text{wall}}. \tag{7.2}$$

The first factor N/σ_x is a measure of the beamstrahlung, the second σ_y depends strongly on the beam quality and the efficiency η of transforming the wall plug power P_{wall} into beam power is dominated by the RF to beam transfer efficiency of the main linac.

The beamstrahlung can conveniently be described with the beamstrahlung parameter Y, the ratio of the average critical energy $\hbar\omega_c$ to the beam energy E:

$$Y = \frac{2}{3}\frac{\hbar\omega_c}{E} = \frac{5}{6}\frac{Nr_e^2\gamma}{\alpha\left(\sigma_x + \sigma_y\right)\sigma_z}. \tag{7.3}$$

Here, α is the fine structure constant, r_e the classical electron radius and γ the relativistic factor of the beam. In the classical limit $Y \gg 1$, which is applicable to the ILC or CLIC at 500 GeV, the number of beamstrahlung photons emitted per beam particle n_γ and their average energy E_γ can be approximated as

$$n_\gamma \approx 2.1\alpha\frac{Nr_e}{\sigma_x + \sigma_y}\frac{E_\gamma}{E} \approx 0.385\frac{Nr_e^2\gamma}{\alpha\left(\sigma_x + \sigma_y\right)\sigma_z}. \tag{7.4}$$

Hence, one uses $\sigma_x \gg \sigma_y$ to maximise luminosity ($\propto N/(\sigma_x\sigma_y)$) while limiting the beamstrahlung ($\propto N/(\sigma_x + \sigma_y) \approx N/\sigma_x$). Typically one aims for $n_\gamma \leq 1 - 2$ to maximise luminosity while maintaining the degradation of the luminosity spectrum due to beamstrahlung comparable to the degradation due to initial state radiation. Hence, the machine is designed such that the optimum value of N/σ_x can be reached.

The vertical beam size depends on the vertical beta-function and emittance at the interaction point $\sigma_y = \sqrt{\beta_y\varepsilon_y/\gamma}$. Hence the vertical emittance is minimised as much as possible, with limits arising from the lattices designs and dynamic and static imperfections in the beam transport system. In addition one aims to minimise the beta-function. However, a beta-function smaller than the bunch length leads to a rapidly increasing beam size just before and after the collision point still during the collision with the other bunch. Ignoring beam-beam forces, the optimum choice is $\beta_y = \sigma_z/4$ due to this so-called hourglass effect. The luminosity would only be 20% larger than for the more relaxed value of $\beta_y = \sigma_z$. The beam-beam force strongly modifies the collision and impacts the optimum choice of vertical beta-function and the longitudinal position of beam waist [36]. Pinching of the beams is more effective for larger vertical beta-functions, For ILC and CLIC parameters the luminosity enhancement factor is strongly reduced if the beta-function is pushed below the bunch length resulting in an optimum choice of about $\beta_y = \sigma_z$. It is also advantageous to focus the beams slightly before the collision point as this further improves the luminosity enhancement.

A small value of σ_y also has a strong impact on the beam-beam collision dynamics and tolerances. The beam-beam jitter must be significantly smaller than σ_y, but the disruption can tighten the tolerance even more. The strength of the pinch

effect can be described using the disruption parameters D_x and D_y:

$$D_{x,y} = \frac{2Nr_e\sigma_z}{\gamma\sigma_{x,y}\left(\sigma_x + \sigma_y\right)}. \tag{7.5}$$

If $D_{x,y} \ll 1$ each beam acts as a thin lens on the other beam with a focal length $f_{x,y} = \sigma_z/D_x$ close to its centre. If $D_x \gg 1$ the beam particles oscillate in the field of the other beam; ILC and CLIC have $D_x < 1$ and $D_y \gg 1$. For $D_y \geq 15 - 20$ the beam-beam interaction becomes unstable. In this case very small beam-beam offsets lead to a large loss of luminosity.

In order to increase the wall plug to beam power efficiency, η, two different strategies exist. The first is to use superconducting structures to minimise the RF losses in the structure itself. The second it to use normal conducting structures but to increase the structure impedance and the beam current as much as possible to maximise the power transfer to the beam. A limit arises from single and multi-bunch beam instabilities, see Sect. 7.5.

At multi-TeV energies, the beamstrahlung parameter is much larger, $Y \gg 1$, which slightly changes the functional dependence of the luminosity on the number of beamstrahlung photons to

$$L \propto n_\gamma^{\frac{3}{2}} \frac{\sqrt{\gamma}}{\sqrt{\sigma_z}} \frac{1}{\sigma_y} P_\mathrm{b}. \tag{7.6}$$

However, the fundamental considerations remain unchanged.

The beam-beam interaction is an important source of background. The disrupted beam and the beamstrahlung photons need to be extracted from the detector without large losses, this requires typically an exit hole of a few milliradian. In addition secondary particles are produced.

The collision of beamstrahlung photons and beam particles produces low energy electron-positron pairs, a process called incoherent pair production. The number of these particles per bunch crossing can be of the order of 10^5–10^6. They are an important source of background in the innermost layer of the vertex detector and define a lower limit for its radius. Most of the particles go into the forward region of the detector.

In a similar fashion, hadrons can also be produced in the collision, with a rate ranging typically from one event every few bunch crossing to a few events per bunch crossing. Most of the tracks of these events go into the forward region but they can impact the jet reconstruction.

At high beam energies, if $Y \gg 1$, beamstrahlung photons and the virtual photons accompanying the beam particles can turn into electron-positron pairs due to the strong beam fields, a process referred to as coherent pair production [37]. The number of pairs can be a significant fraction of the number of beam particles. These particles can lead to background in the forward region, depending on the detector design.

7.3 CLIC & ILC

J. P. Delahaye · M. Ross · S. Stapnes

7.3.1 Introduction

The case for an e+e− collider to explore the physics opened up by the discovery of the Higgs boson is widely accepted. More generally, with the completion of the Standard Model the energy scales needed to explore it in great detail are well established. Two alternative technologies for linear e+e− colliders are being pursued, with different potential energy reach and performance considerations:

- The International Linear Collider (ILC) [38] being proposed in Japan with an initial energy of 250 GeV has the potential to study the Higgs sector in great detail. The ILC is based on beam acceleration by RF Super-Conducting cavities and is prepared as an international project lead by Japan. The ILC Technical Design Report (TDR) [39] was published in 2012 focusing on a 500 GeV machine. Recently a 250 GeV initial stage has been defined [40].
- The Compact Linear Collider (CLIC) [41] study is exploring the possibility of a Linear Collider with a Multi-TeV energy range through the development of Two Beam Acceleration, a novel technology. Normal conducting 12 GHz X-band accelerating structures are used. The study is carried out an international collaboration hosted by CERN. The CLIC Conceptual Design Report (CDR) was published in 2012 [42]. In 2014 an initial stage at 380 GeV was defined and is currently the main focus of the study [43].

These two studies, with the basic parameters shown in Table 7.2, aim to devise appropriate facilities to complement the LHC in the e+e− area. A collaboration between CLIC and ILC that takes advantage of the overlapping portions of the two schemes has proven to be extremely fruitful.

The main challenge for both concepts is reliable and power efficient acceleration, hence the focus on RF technology developments. Secondly, the required luminosity of about 1.5×10^{34} cm^{-2} s^{-1} is a major challenge. It requires collisions of powerful beams with extremely small beam dimensions (a few nm in the vertical plane). Cost is another key factor, both ILC and CLIC aiming for project-costs comparable to LHC [44].

7.3.2 ILC Design

The design of the International Linear Collider (ILC) is based on 1.3 GHz Super-Conducting RF technology (SCRF). The configuration of the linac power and utility

Table 7.2 Basic parameters for ILC and CLIC

	ILC	CLIC
Centre-of-mass energy	250 GeV (upgradable to 1 TeV)	380 GeV (upgradable to 3 TeV)
Total luminosity ($cm^{-2}\ s^{-1}$)	1.4×10^{34}	1.5×10^{34}
Total site length (km)	20	11
Loaded accel. gradient (MV/m)	31.5 (35)	72 (100)
Main linac technol. & RF frequency	Super-conduct @ 1.3 GHz	Normal-conduct @ 12 GHz
Beam power/beam (MW)	5	3
Bunch charge ($10^9 e^{+/-}$)	20	5.2
Bunch separation (ns)	554	0.5
Beam pulse duration (μs)	722	0.176
Repetition rate (Hz)	5	50
Hor./vert. norm. emitt ($10^{-6}/10^{-9}$)	5/35	0.95/30
Hor./vert. IP beam size (nm)	520/8	150/3
Beamstrahlung photon/electron	1.9	1.5
Total power consumption (MW)	130	200

infrastructure is based on klystron sources and waveguide distribution. A train of 1312 bunches is accelerated during a ~1.6 ms macro-pulse, corresponding to the beam-pulse duration plus cavity fill-time, at a repetition rate of 5 Hz. The average gradient foreseen is 31.5 MV/m but on-going R&D opens for the possibility to increase to 35 MV/m with higher Q cavities (see Sect. 7.3.4). The cryo-modules that make up the main linacs are 12.65 m long. There are two types: a module with nine 1.3 GHz nine-cell cavities and a module with eight nine-cell cavities and one superconducting quadrupole package located at the centre of the module.

The RF power is provided by 10 MW multi-beam klystrons each driven by a 120 kV Marx modulator. The 10 MW klystrons has achieved the ILC specifications and is now a well-established technology with several vendors worldwide.

The long time scale of the 722 μs macro-pulse, with 554 ns between bunches, provides the time needed for effective intra-train trajectory, energy and interaction region collision feedback resulting in very relaxed mechanical vibration tolerances. Accelerating cavity positioning tolerances are also relaxed due to the large 70 mm diameter clear aperture of the accelerating cavities.

The ILC overall layout is shown on Fig. 7.2. The figure shows two centrally-positioned detectors and the electron and positron damping rings. It also shows the mid-linac undulator-based positron source.

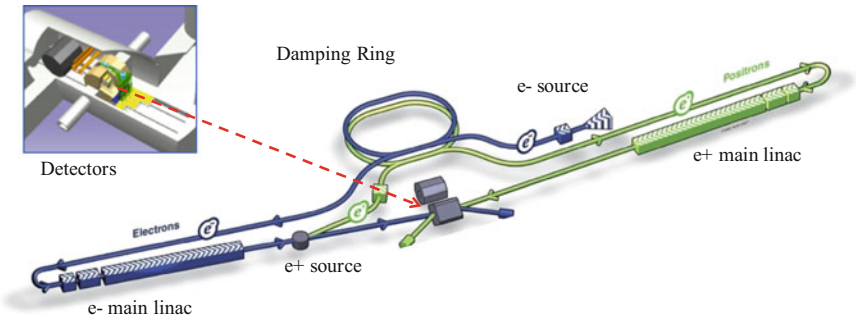

Fig. 7.2 ILC overall layout with the central region expanded

7.3.3 CLIC Design

The CLIC design is based on a novel Two Beam Acceleration (TBA) scheme where a high intensity drive beam running all along the linacs accelerating the main beams. The CLIC main linacs are made of normal-conducting structures resonating at RF frequency of 12 GHz with average accelerating fields of 72/100 MV/m resulting from an overall cost/performance optimisation at 380 GeV/3 TeV, respectively. The accelerating field results from a cost optimisation primarily being a trade-off between the linac extension and the required RF power. The X-band frequency of 12 GHz also results from a trade-off between the required RF power, scaling with inverse square of RF frequency, and the corresponding wake-fields which limit the charge per bunch, therefore the luminosity.

The RF power which is necessary to feed the main linac accelerating structures with high field is efficiently generated by the TBA scheme where the energy of a high intensity drive beam is converted into RF power by specially designed Power Extraction and Transfer Structures (PETS). The 100 A drive beam is generated from a 148 μs long train of bunches accelerated by 20 MW 1 GHz klystrons in a 2.4 GeV normal conducting linac at low intensity and low frequency working in fully loaded mode. For the initial stage of CLIC at 380 GeV one single drive beam at 2 GeV is needed with shortened bunch train, while at 3 TeV two will be needed. The drive-beam trains are compressed in a delay loop and two combiner rings thus multiplying the beam intensity and frequency by a factor 24 and providing series of trains with the required 100 A current and 12 GHz bunch repetition frequency. Each train is used to power one 878 m long sector of the main linac. Upgrade in energy by adding sectors powered by additional drive beam generated by the same drive beam generation complex is particularly cost effective.

The overall layout is shown in the left part of Fig. 7.3 whereas the principle of the two beam scheme is displayed on the right.

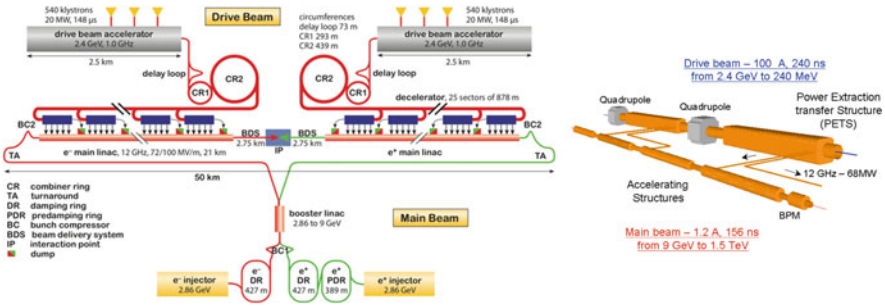

Fig. 7.3 CLIC two-beam scheme (left) and overall layout (right). In the case of a 380 GeV initial phase only one drive-beam is needed and the layout is simplified accordingly

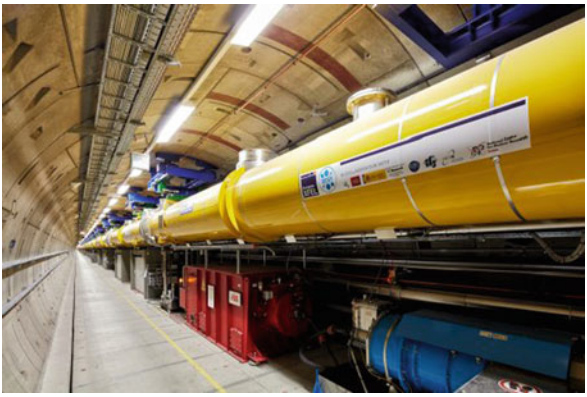

Fig. 7.4 The E-XFEL linac (©European XFEL/Heiner Müller-Elsner)

7.3.4 On-Going or Recent R&D

7.3.4.1 ILC Specific

High quality ILC-style SCRF modules are built in all three regions, Americas, Asia and Europe. Furthermore, linacs based on SCRF technology have been/are being constructed, the largest being the 1.7 km European XFEL [45] now in operation with more than 100 cryo-modules (Fig. 7.4). In the US the LCLS II with around 40 cryo-modules at SLAC [46] is being constructed aiming for first beam in 2020. These large scale projects have firmly established the industrial capabilities for SCRF module production.

For ILC slightly higher gradients are needed than for these projects and recent R&D and results for high Q cavities provide promises of gradient and/or efficiency gains [47].

Since 2012 when the Japanese particle physics community expressed the wish to host the ILC [48] site specific studies have been pursued with high priority. These

include civil engineering studies including surface installations, as well as studies of local infrastructure and capabilities.

R&D is continuing on various non-linac related subsystem technologies, such as the positron source, damping rings, and beam delivery/final focus. Many of these R&D topics are common with the CLIC studies and are performed in close collaboration with CLIC teams.

7.3.4.2 CLIC Specific

The feasibility of the novel two-beam scheme has been addressed in the CLIC Test Facility (CTF3) which consists of a complex of accelerators for drive beam generation and experimental studies [49]. The drive beam is used to test the Two Beam Acceleration scheme accelerating a probe beam with a gradient well above 100 MV/m. The stability of the drive-beam itself has been another major verification study in CTF3, as well as studies of prototype RF structures, quadrupoles, instrumentation, vacuum, beam alignment and stabilisation (Fig. 7.5).

The accelerating gradient of 100 MV/m with the specified breakdown rate of 3×10^{-7}/pulse/m has been demonstrated in test-stands where prototype test-structures are conditioned to the required power, pulse-lengths and breakdown rate. The requirement for the breakdown rate—these are discharges on the structure surface with the potential of disturbing the beam—is set to cause less than 1% luminosity loss in a 3 TeV machine.

Fig. 7.5 The CTF3 test facility at CERN, which has demonstrated CLIC's novel two-beam acceleration technology (image credit: Maximilien Brice – CERN)

Technological developments are pursued for all critical elements of the machine. Of particular relevance are novel methods of alignment in the micron range and stabilisation in the nano-meter range. Power reductions studies with high efficiency klystrons and permanent magnets are important R&D activities. Civil engineering and infrastructure studies have been done to establish the cost and schedule of the project implementation.

Also in the case of the normal conducting technology XFELs linacs provide important industrial lessons, so far using S or C-band technology. X-band technology is now widely considered for future compact linac installations [50].

7.3.5 Common Issues and Prospects

Apart from the linacs based on different RF-technologies, ILC and CLIC have similar technology challenges for several sub-systems. This is especially so for the beam delivery system, the machine detector interface and the civil engineering & conventional facilities. To take advantage of the overlapping aspects of the two studies, common working groups have been set-up and actively address common issues for both studies including beam dynamics, low beam emittance generation, positron generation, beam delivery system as well as cost and schedule. Issues of low emittance beam generation, electron cloud collective instabilities, emittance conservation studies, and beam optics for the interaction region are being tested in test facilities supported by linear collider groups, notably in the CESR-Test Accelerator at Cornell, FACET and SLAC, and the Accelerator Test Facility (ATF2) at KEK [51–53].

The 250 GeV ILC project is currently being evaluated for implementation in Japan. During 2018 one is expecting that Japan can conclude this evaluation which will determine if the project will move forward towards realisation. Such a machine could start operation in the early 2030s. The CLIC collaboration will submit a Project Implementation Plan by the end of year, describing a project that could come into operation after completion of the LHC programme in the mid 2030'ies.

7.4 Accelerating Structures Design and Efficiency

A. Grudiev · A. Yamamoto

In linear accelerators, beam is accelerated by accelerating structures made of a chain of cavities (cells) fed with RF power establishing an electromagnetic field from which part of the energy is transferred to the beam.

The efficiency of a cavity to produce an accelerating field with given RF power is defined by the shunt impedance R. This is equivalent to Ohm's law where the resistance is the proportionality factor between the square of the voltage and the

power loss as given by:

$$V_{\text{acc}}^2 = RP, \tag{7.7}$$

where V_{acc} is the accelerating voltage per cavity, R is the shunt impedance per cavity, and P is the RF power loss per cavity [1].

At a given power loss P, the accelerating voltage can be maximised by optimum shape of the cavity and through the use of low-loss cavity-surface material. Therefore the shunt impedance can be divided into two factors, R/Q and Q, as follows:

$$R = \{R/Q\}\, Q, \tag{7.8}$$

where R/Q is the so-called "cavity shape factor", only depending on the cavity shape, and Q is so-called "quality factor of the cavity resonator", mainly depending on the conductivity of the cavity wall. This brings:

$$V_{\text{acc}}^2 = \{R/Q\}\, QP. \tag{7.9}$$

The R/Q value can be calculated using several available cavity codes or can be measured, and compared with a simple cavity that can be evaluated analytically. Superconducting cavities have a typical value of $R/Q = 100\ \Omega$ per cell. The shunt impedance R and the shape factor R/Q value with normal-conducting cavities must be optimized to reduce the RF power.

The quality factor Q is proportional to the ratio of the stored energy and the RF power loss,

$$Q = \omega U/P, \tag{7.10}$$

where $\omega = 2\pi f$ is the angular frequency, U is the stored energy, and P is the RF power loss dissipated in the cavity wall. A typical value for Q is 1×10^{10} for niobium superconducting cavities at 1.3 GHz and 1.8 K [1].

Assuming one cell length, l, is 0.5 wavelength, we can calculate the RF power loss per meter:

$$P/l = \left(V_{\text{acc}}^2/l\right) / \{(R/Q)\, Q\} = E_{\text{acc}}^2 l / \{(R/Q)\, Q\}. \tag{7.11}$$

Historically, normal conducting structures have been in use since the very beginning of RF acceleration covering the whole range of applications from very low frequency drift tube linac structures up to very high frequency travelling wave accelerating structures. Typically, normal conducting structures handle high peak power to provide high gradient and/or to support high beam loading but the pulse length is limited by the ohmic heating of the copper walls. To overcome this limitation at least in some cases, superconducting accelerating structures are

being developed for several decades, in the frequency range from few hundreds of megahertz to a few gigahertz, with improving performances as described below in Sect. 7.4.2.

7.4.1 Normal Conducting Accelerating Structures

In normal conducting (NC) linacs, acceleration of charged particles using RF power is typically done in a chain of cavities (cells) which are strongly coupled and where the electromagnetic wave propagates through the cells from the input to the output of the structure. This allows a single RF source to feed many cells via single input coupler thus minimizing the feeding waveguide network. The chain of cells forms a periodic structure which, in the simplest case of a disk-loaded circular waveguide, is shown in Fig. 7.6a where the input and output couplers allow to feed the structure with RF power and extract the remaining RF power out. The property of an electromagnetic wave propagating in an infinitely long periodic structure of period d is described by dispersion curves $\omega(k_z)$, so called the Brillouin diagram as shown in Fig. 7.6b by the thick solid line. If the structure is excited at a frequency f_0 inside the passband (shown in gray in Fig. 7.6b), then the wave propagates along the structure with an RF phase advance per cell: $0 < \varphi_0 < \pi$. A travelling-wave accelerating structure is a structure where the wave is matched at both input and output ends. Since most of the normal conducting lepton linacs are based on this type of accelerating structures we will restrict ourselves to this case.

The following synchronism condition is fundamental for acceleration in periodic structures and must be satisfied in order that all cells contribute in phase to beam acceleration:

$$v_{ph} = v_p, \tag{7.12}$$

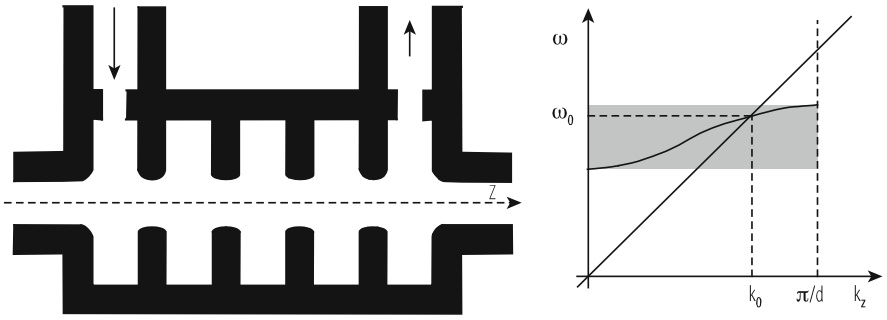

Fig. 7.6 Schematic geometry of a travelling wave accelerating structure with input and output coupler cells is shown in (**a**). Brillouin diagram for a periodic structure of period d is shown in (**b**), where $\omega_0 = 2\pi f_0$ is the operating frequency, $k_0 = \varphi_0/d$ is the propagation constant, and $\omega_0 = \omega(k_0)$

where v_{ph} is the phase velocity of the wave excited at operating frequency and v_p corresponds to the velocity of the charged particle. Ultra-relativistic case with $v_p = c$, the speed of light, is considered below. In this case, the beam line with a slope c (strait line in Fig. 7.6b as $\omega = v_p k_z$) must intersect the dispersion curve at the operating point: $(f_0; \varphi_0)$ on the Brillouin diagram in order to satisfy the synchronism condition (7.12). The slope of the dispersion curve provides another important parameter of the wave propagating in the structure, the so called group velocity:

$$v_g = \frac{\partial \omega}{\partial k_z}, \tag{7.13}$$

which can also be expressed using the cell stored energy U and power flow through the cell iris aperture P_z:

$$v_g = \frac{P_z d}{U}. \tag{7.14}$$

The stronger the coupling between the cells the higher the group velocity and the faster energy propagates along the structure. Combining Eqs. (7.9, 7.10 and 7.14) yields expression for the power flow along the travelling-wave structure which is needed to maintain an accelerating gradient $E_{\mathrm{acc}} = V_{\mathrm{acc}}/d$:

$$P_z = v_g \frac{E_{\mathrm{acc}}^2}{\omega R'/Q}, \tag{7.15}$$

where $R^{'} = R/d$ is the shunt impedance per meter length. For a given working point $(f_0; \varphi_0)$, the group velocity, the Q-factor and the R-upon-Q fully describe the accelerating properties of the cell. In so-called constant impedance, the geometry of all cells is identical and the three above parameters are identical in all cells. In practice, the so-called constant gradient structures are used. In these structures, the geometry of the cells is tapered in order to maintain $E_{\mathrm{acc}}(z) \approx const$. This is achieved by reducing the group velocity along the structure to compensate the reduction in power flow along the structure which is caused by two terms: ohmic losses according to Eq. (7.15) and power gained by the beam of a current $I = qf_b$, where q is the bunch charge and f_b is the bunch repetition frequency. In this case, the energy conservation law yields an equation for the power flow along the structure:

$$\frac{dP_z}{dz} = -\frac{P_z \omega}{v_g Q} - E_{\mathrm{acc}} I. \tag{7.16}$$

The distribution of accelerating gradient $E_{\mathrm{acc}}(z)$ along the structure is obtained by solving Eqs. (7.15 and 7.16) for a given input power P_{in}. Integrating it over the structure length L gives the overall structure energy gain:

$$V_{AS} = \int_0^L E_{\mathrm{acc}}(z)dz. \tag{7.17}$$

Then the steady-state RF-to-beam efficiency is defined as following:

$$\eta_0 = \frac{V_{AS}I}{P_{in}}. \tag{7.18}$$

For linacs operating in pulsed mode, the structure must be filled on each pulse before beam is injected. Filling time of the structure is defined as

$$t_f = \int_0^L \frac{dz}{v_g(z)}. \tag{7.19}$$

In this case, RF-to-beam efficiency, η, is reduced by the ratio of the bunch train length $t_b = N_b/f_b$, where N_b is the number of bunches and the RF pulse length $t_p = t_b + t_f$:

$$\eta = \eta_0 \frac{t_b}{t_p}. \tag{7.20}$$

A few examples of normal-conducting travelling wave cavity parameters are provided in Table 7.3.

Table 7.3 Examples of normal-conducting travelling wave cavities

	SLC [54]	CTF3 [55]	CLIC-ML [56]
Frequency (GHz)	2.9	3	12
Average gradient (MV/m)	17	7	100
Average Q	13,000	12,500	5640
Current (A)	Two bunches e+e−	4	1
Repetition rate (Hz)	180	50	50
Pulse width (μs)	0.82	1.6	0.24
RF-to-beam efficiency (%)	2	90	28
# cell/cavity unit	85 + 2	32 + 2	26 + 2
Status	In operation	In operation	R&D

7.4.2 *Superconducting Accelerating Structures*

Linear accelerators have benefitted greatly through the use of superconducting radio-frequency (SCRF) cavity technology [1, 57]. This technology, when applied in standing-wave RF operation, provides the following important advantages:

- Small RF surface resistance and large quality factor, Q, resulting *long pulse operation*, with a range of 1 ms, and much higher duty factor in beam acceleration.
- Lower operational frequency with enlarged beam-apertures in the range of ~70 mm diameter, (1.3 GHz), resulting in large acceptance and providing practical solutions for *very intense* beams.

Two salient characteristics of superconducting cavities are (1) the average accelerating field gradient E_{acc} and (2) the intrinsic quality factor Q. Quality factor Q is a universal figure of merit for resonators and is defined in the usual manner as the ratio of the energy, U, stored in the cavity to the power, P_c, lost in one RF period. Q depends on the microwave surface resistance of the metal. In general, one would like to have as high accelerating field and as high Q as possible.

The strongest incentive to use superconducting cavities in an accelerator is that continuous wave (CW) mode or high duty factor (>1%) operation is practical. For CW operation power dissipation in the walls of a copper structure is substantial and often not possible. Here superconductivity comes to the rescue. The microwave surface resistance of a superconductor is typically five orders of magnitude lower than that of copper, and therefore the Q value is five orders of magnitude higher [58]. The above advantages may be of benefit even though superconducting technology requires low temperature (1.8 K) cryogenic system operation, resulting additional power consumption, discussed below.

Figure 7.7a shows a schematic cavity shape of a normal-conducting multi-cell cavity (top), which represents larger impedance to the beam due to the small beam

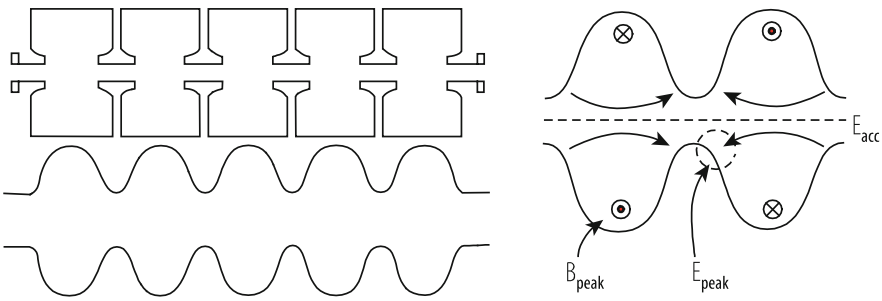

Fig. 7.7 (**a**) A comparison of cylindrical shaped normal-conducting RF cavity (top) and elliptical shaped superconducting RF cavity (bottom), and (**b**) electric and magnetic field profile in the elliptical cavity structure [1, 2]

holes and nose cones, and a schematic shape of a superconducting multi-cell cavity (bottom). The corresponding electromagnetic field profile inside an elliptical cavity is shown in Fig. 7.7b [1, 2].

The RF loss is proportional to the square of the surface current and proportional to the resistivity. For a superconducting cavity, the microwave surface resistivity is several orders of magnitude smaller than that of Cu, although it is not zero. The shape of a superconducting cavity is optimised for properties such as: (1) reduced excitation of higher order harmonics by the beam, (2) reduced surface magnetic field to enhance the critical limit of the resultant superconducting to normal-conducting phase transition, (3) reduced surface electric field to suppress field emission, and (4) reduced multipacting behaviour [59–61]. The large iris opening and elliptical shape result from these considerations.

Following Eq. (7.11), an RF power loss per meter of ~0.1 W/m is generated in an accelerating cavity gradient of 1 MV/m, and it is proportionally increased with .square of the frequency.

The above RF power loss dissipated into the 1.8 K cryogenic fluid needs to be converted to an AC power load at room temperature using a total cryogenic efficiency estimate, η_{cr}, which includes the 'Carnot efficiency' and the 'thermodynamic efficiency as follows:

$$\eta_{\mathrm{cr}} = \eta_{\mathrm{c}}\eta_{\mathrm{d}} = (P_{1.8\mathrm{K}}/P_{300\mathrm{K-i}})\,(P_{300\mathrm{K-i}}/P_{300\mathrm{K-r}})\,, \tag{7.21}$$

where η_{c} is the 'Carnot efficiency', η_{d} is the 'thermodynamic efficiency' for the compressor work at 300 K [2]. Assuming η_{c} is ~1/(300/1.8) and η_{d} is ~0.2 (typical for large scale refrigerators), the total cryogenics efficiency η_{cr} can be ~1/800. Including this effect in the estimate of power loss, the relative RF power loss saving factor of superconducting cavities, (surface resistance ~10^{-5} lower than normal-conducting cavities), may be approximately two orders of magnitude better in AC power consumption performance for a CW operation. Therefore, superconducting cavity technology enables the nearly entire (>99%) RF power to be transmitted to the beam from the power source,

However, in case of the pulsed operation, which is the usual mode of normal-conducting cavity operation, general power loss should be evaluated including a duty factor, and is given by

$$(\omega U/Q) \times (\text{pulse length}) \times (\text{repetition rate}) = (\omega U/Q) \times (\text{duty factor})\,. \tag{7.22}$$

The pulse duration is typically in the μsec range in case of normal conducting cavity operation, and the duty factor is normally about three orders of magnitude smaller for normal-conducting cavity operation, compared with the superconducting cavity operation. It results in the general power balance between the normal-conducting cavity and superconducting cavity operation become in similar level, with including the total cryogenic efficiency for the superconducting cavity operation. On the other hand, it should be noted that a pulse duration in the level of msec,

Table 7.4 Summary of superconducting cavities in operation, and planned [65, 66]

	FLASH	European-XFEL	ILC-ML
Gradient (MV/m)	18–35	23.8	31.5
Q	5×10^9 to 1×10^{10}	1×10^{10}	1×10^{10}
Current (mA)	1–9	5	6
Repetition rate (Hz)	5	10	5
Pulse width (μs)	800	650	730
# cell/cavity unit	9	9	9
Status	In operation	In operation	Planned

thus three order magnitude longer than that of the normal-conducting cavity, would be much helpful in other linear collider sub-system such as detectors and feedback system. A superconducting cavity system may be expected to operate with more than two times better efficiency, in CW operation than that of the normal conducting cavity system. However, the power consumption in pulsed operation is less different in either case.

The superconducting cavity intended for use in high-energy accelerators was designed for operation at 1.3 GHz with a cell length of 115.4 mm. The 9-cell elliptical cavity was designed and developed for the FLASH/TESLA Test Facility program at DESY [62], and has become a standard for further programs such as the European XFEL program [63] and for the ILC project [64]. Table 7.4 gives a summary of superconducting cavity operation in FLASH, planned operation at European-XFEL, and planned for ILC [65, 66]. Superconducting cavity technology is expected to advance substantially through further optimization of cavity materials, shapes (TESLA, Low-Loss, Re-entrant), and cost-effective fabrication techniques [57, 59–61, 65–68].

7.5 Wakefields and Emittance Preservation

A. Latina

Wakefields induced by particles in high impedance environment interact with the following particles and can therefore affect the beam quality. They can be described in either the time domain, using the wake-potential W, or in the frequency domain, using the impedance Z. Analytical approximations to describe wakefields due to resistive walls or geometry variations in periodic accelerating structures exist. In case of complex geometries, however, the analytical computation of wake-potentials and impedances must be performed numerically. In the following paragraphs, we provide models for short- and long- range wakefields and describe their impact on the beam. The symbols used in the following paragraphs are defined in Table 7.5. The unit 1/m in the wakefield functions indicates that the effect is normalized to the length of the generating element. The unit 1/mm (and its second power) relates to the

Table 7.5 Symbols and constants used in the text

Symbol	Description	Notes	Symbol	Description	Notes
e	Absolute electron charge	1.6×10^{-19} C	L_0	Length of the linac	(m)
c	Speed of light	299,792,458 m/s	k_β	Average lattice focusing strength	(1/m)
N	Bunch population	Number of particles	Z	Impedance	(Ω)
q	Bunch charge	$q = Ne$	$W_{\parallel,\,0}$	Wake: longitudinal monopole	(V/C/m)
σ_z	r.m.s. bunch length	(m)	$W_{\perp,\,1}$	Wake: transverse dipole	(V/C/m/mm)
E	Bunch energy	(GeV)	$W_{\perp,\,2}$	Wake: transverse quadrupole	(V/C/m/mm^2)
l_b	Bunch-to-bunch distance	(m)	V	Cavity voltage	$V = GL$
L	Length of a cavity	(m)	G	Cavity accelerating gradient	(V/m)

transverse offset of the exciting charge. For example, the transverse and longitudinal momentum kicks experienced by a charge q following at a distance z a charge Q, due to the transverse dipole and the longitudinal monopole modes, are respectively $\Delta \overrightarrow{p}_{\perp} = -qQL_{structure} \overrightarrow{r}_{\perp} W_{\perp,1}(z)$, and $\Delta \overrightarrow{p}_{\parallel} = -qQL_{structure} W_{\parallel,0}(z)$, where $L_{structure}$ is the length of the structure and $\overrightarrow{r}_{\perp}$ is the (small) transverse offset of the exciting charge.

7.5.1 Short-Range Wakefields

The wake-functions of a periodic accelerating structure have been parameterized by a number of authors. Here we present a convenient formula for the longitudinal and the transverse component of the wake-potential, $W_{\parallel}$, provided by Bane et al. [69]:

$$W_{\parallel} = \frac{Zc}{\pi a^2} \exp\left(-\sqrt{\frac{s}{s_0}}\right), \text{ and } s_0 \approx 0.41 \frac{a^{1.8} g^{1.6}}{d^{2.4}}, \tag{7.23}$$

$$W_{\perp,1} = 4\frac{Zc}{\pi a^4} s_0 \left(1 - \left(1 + \sqrt{\frac{s}{s_0}}\right)\right) \exp\left(-\sqrt{\frac{s}{s_0}}\right), \text{ and } s_0 \approx 0.169 \frac{a^{1.79} g^{0.38}}{d^{1.17}},$$

where s is the distance from the source charge, a is the radius of the iris aperture, g is the interior cell width and d is the cell period (i.e. $g = d - h$ where h is the disc thickness); Z is the impedance of the medium, typically 377 Ω for an evacuated accelerating structure.

7.5.2 Long-Range Wakefields

The long-range wakefields are usually characterized by a set of cavity modes, obtained numerically. Three numbers (c_m, Q_m, k_m) are necessary to describe a mode. Following Eq. 2.88, in [70], the wake-function for each mode m, is

$$W_{\perp,m}(s) = c_m \frac{R}{Q_m} \exp\left(\frac{k_m z}{2Q_m}\right) \sin(k_m s), \tag{7.24}$$

where c_m is the amplitude of the mode in V/C/m/mm^m, Q_m is the quality factor, k_m is the wake number, and s is the distance from the source to the witness particle and is negative for all particles affected by the wake. Note that $W_{\perp,m}(s)$ is a decaying exponential as expected. The total wake-potential is the sum of all modes.

7.5.3 Single-Bunch Wakefield-Induced Effects

7.5.3.1 Beam Loading

The electromagnetic interaction between the bunch tail and the wakes induced by the bunch head, causes the tail to radiate and lose energy. This decelerating effect is called *beam loading*. The energy loss experienced by each particle is estimated by adding to the self-generated wake the decelerating voltage due to the upstream generated wakefields:

$$\Delta E = -eL \sum_i \left[\frac{1}{2} |q_i| W_\parallel(0) + \sum_{\forall j / z_i < z_j} \left\{ \left| q_j \right| W_\parallel \left(z_{ij} \right) \right\} \right], \tag{7.25}$$

where $z_{ij} = z_j - z_i$ is the distance between the ith and the jth macroparticles; the inner summation runs over all particles preceding q_i, i.e. with $z_i < z_j$. Notice that the energy loss due to the self-generated wakefield, in $z = 0$, is *half* the energy loss given by the upstream generated wakefield. This is the *fundamental theorem of beam loading* [71].

7.5.3.2 Wake-Induced Energy Spread

Since the decelerating voltage in Eq. (7.2) varies along the bunch, an RMS energy spread arises. An estimate of this wakefield-induced energy spread can be obtained considering $W_\parallel$ in Eq. (7.23) and a bunch modeled with two macro-particles located at $z = 0$ and $z = 2\sigma_z$ respectively,[1] each with charge $q/2$. The decelerating voltage experienced by the two particles is

$$\begin{aligned} \Delta V_1 &= \tfrac{1}{2} \tfrac{qL}{2} W_\parallel(0), \\ \Delta V_2 &= \tfrac{1}{2} \tfrac{qL}{2} W_\parallel(0) + \tfrac{qL}{2} W_\parallel(2\sigma_z) = \tfrac{1}{2} \tfrac{qL}{2} W_\parallel(0) \left(1 + 2\mathrm{e}^{-\Delta}\right), \text{ with } \Delta = \sqrt{2\sigma_z / s_0}. \end{aligned} \tag{7.26}$$

The two particles experience two different energy losses: ΔE_1 and ΔE_2 (where $\Delta E = -e\Delta V$), this introduces energy spread within the bunch:

$$\delta E = e \frac{qL}{2} W_\parallel(2\sigma_z). \tag{7.27}$$

[1] This gives the overall distribution an RMS length of σ_z.

7.5.3.3 Energy Spread Compensation

To compensate for the wake-induced energy spread, one can adjust the RF phase offset ϕ_{RF} (at the cost of a slight reduction of the acceleration rate), so that the change in energy gain equals the change in wakefield deceleration. In the approximation $V \gg qLW_{\parallel}(0)$, $\sigma_z \ll s_0$, and $\sigma_z \ll \lambda$ the result is [71]

$$\phi_{RF} = \frac{qLW_{\parallel}(0)}{8\pi V}\frac{\lambda}{\sigma_z}, \tag{7.28}$$

where λ is the wavelength of the accelerating mode and V its voltage. The residual energy spread after compensation is found from the convolution of the bunch with the longitudinal wakefield and the acceleration RF

$$\frac{\Delta E}{E} \approx \frac{1}{4}\frac{qW_{\parallel}(0)}{G}. \tag{7.29}$$

7.5.3.4 Single-Bunch Beam Break-up

If the beam is traversing off-center an acceleration cavity, the bunch head can excite a transverse dipole wakefield $W_{\perp,1}$ that causes transverse deflection of the tail. This deflection affects the tails' betatron motion and can lead to a transverse beam break-up. Using a two-particle bunch model, the oscillation amplitude of the bunch tail relative to the head, at the linac end, is characterized by the dimensionless growth BBU parameter [71, 72]:

$$T_{\mathrm{BBU}} = -\frac{eqW_{\perp,1}(2\sigma_z)}{4k_\beta}\frac{L_0}{L}\frac{2}{\sqrt{E_i E_j}}. \tag{7.30}$$

Here we assume a lattice design where $k_\beta \approx const$ and $\beta \approx \gamma^2$. Equation (7.6) holds also in case of no acceleration, with $1/E$ replacing $2/\sqrt{E_i E_j}$. The BBU parameter can be interpreted as the following: if a beam is injected with a certain betatron oscillation, the transverse wake-functions cause an oscillation of the tail that increases by a factor T_{BBU} long the linac. BBU instability can be mitigated by using BNS damping.

7.5.3.5 Single-Bunch BNS Damping

The defocusing effect of $W_{\perp,1}$ can be compensated by increasing the focusing strength of the tail particles, from k_β to $k_\beta + \Delta k_\beta$. To do this, RF quadrupoles with rapidly varying field can be used, or the bunches can be offset with respect to the crest of the RF wave so that the tail acquires less energy than the head. Using a

two-particles model, the equation of the motion for the trailing particle is [71, 72]

$$x_2''(s) + \left(k_\beta^2 + \Delta k_\beta^2\right) x_2(s) = -\frac{eq\, W_{\perp,1}\,(2\sigma_z)}{2E} x_1(s). \tag{7.31}$$

BNS damping is achieved if the "auto-phasing" condition is met,

$$\left(1 + \frac{\Delta k_\beta}{k_\beta}\right)^2 = 1 + \frac{2T_{\mathrm{BBU}}}{k_\beta L_0}. \tag{7.32}$$

BNS damping should be applied at low energies, where the instability is stronger. In this regime, the energy reducing effect of the longitudinal wakefield actually helps to maximize BNS damping.[2]

7.5.4 Multi-Bunch Wakefield-Induced Effects

7.5.4.1 Multi-Bunch Beam Break-Up

Multi-bunch BBU leads to an amplification of the incoming trajectory jitter to cause trailing bunches to be strongly deflected transversely. Each bunch can be assimilated to a point charge. For n equally-charged, equally-spaced bunches, each bunch represented by a single macroparticle with a charge Ne, the equation of motion is

$$x_n'' + \frac{dE}{ds}\frac{1}{E}x_n' + k_\beta^2 x_n = -\frac{eq}{E}\sum_{i=1}^{n-1} W_{\perp,1}\left((n-1)\, l_B\right) x_i. \tag{7.33}$$

A difference from the single-bunch BBU is that $W_\perp$ is now dominated by one or few resonators having large shunt impedance Q_m (see Eq. (7.1)).

7.5.4.2 Control of Multi-Bunch BBU

The multi-bunch BBU is mitigated by minimizing the long-range transverse wakefield in the structure design. Assuming the Daisy chain model, the criterion for little or no blow-up is

$$\left|\frac{eq\, W_{\perp,1}\,(l_B)}{ek_\beta}\frac{L_0}{L}\right| \frac{2}{\sqrt{E_i E_j}} < 1, \tag{7.34}$$

where $W_{\perp,\,1}(l_B)$ is the wakefield at the following bunch (see Sect. 4.3 in [73]).

[2] Toward the end of the linac, at high beam energies, the beam break-up effect becomes small, and the bunch should be moved ahead of the crest to reduce the energy spread in the beam.

7.6 Focusing at Interaction Point

A. Seryi · R. Tomás García

7.6.1 Final Focus Design

The main task of a Final Focus (FF) system is to focus the beams to the small sizes required at the interaction point (IP) of a Collider. To achieve this, the FF forms a large and almost parallel beam at the entrance to the final doublet (FD), which contains two or more strong quadrupole lenses. However, even for a beam with a minor energy spread of a fraction of a percent, the focused beam size will be diluted by the chromaticity of these strong lenses. The design of a FF is therefore driven primarily by the necessity of compensating the chromaticity of the FD.

There are two primary approaches for chromaticity compensation—the non-local scheme, implemented particularly at FFTB [74] and B-factories [75, 76] and the local compensation Scheme [77] at ATF2 [78, 79]. Further developments in optics with smaller vertical beam size and larger chromaticity are also being investigated at ATF2 [80, 81] to explore the feasibility of the local compensation scheme at different chromaticity levels.

In the non-local FF, the chromaticity is compensated in dedicated sections by sextupole magnets placed at maxima of dispersion and beta-functions. The geometric aberrations generated by the sextupoles are cancelled when used in pairs with a minus identity transformation between them.

The non-local FF is built from separated optics blocks with strictly defined functions, and its design and analysis is relatively simple. The major drawback of the non-local FF rests in its required length for multi-TeV colliders. This can be partly mitigated by allowing a smaller peak dispersion function and adding extra sextupoles to the design [82, 83].

Local compensation of chromaticity is achieved by interleaving a pair of sextupole magnets with the quadrupoles of the final doublet, see Fig. 7.8. The dispersion throughout the FD is created by upstream bends, and is designed to cancel at the IP. Geometric aberrations, generated by FD sextupoles, are cancelled by two or more sextupoles located upstream. Sextupoles placed in FD generate second order dispersion, which, however, can be compensated simultaneously with x and y chromaticities provided that half of the total horizontal chromaticity of the whole FF is generated upstream. The second order aberrations are cancelled when the x and y pairs of sextupoles are separated by transfer matrices M with block-diagonal structure $\{A\ 0; 0\ B\}$ where $A = \{f\ 0; c\ -\ 1/f\}$, provided the optics is flexible enough to adjust the coefficients and provide compensation of third and fourth order aberrations. The FF with local compensation requires fewer bends, and allows the design of a 3 TeV CM FF system with about half a kilometre length. The recipe for the design of such final focus is described in [84].

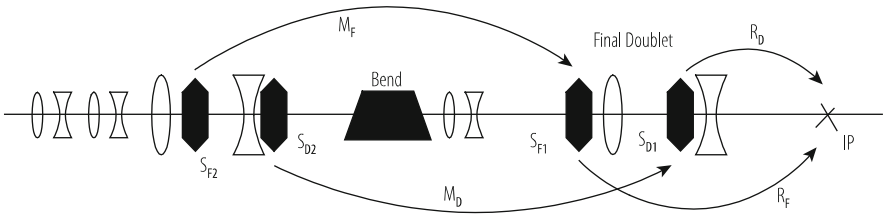

Fig. 7.8 Optical layout of the final focus with local chromaticity correction. The final doublet consists of two quadrupoles (represented by lenses) and two sextupoles (represented by hexagons) to locally cancel the chromatic aberrations. A replica of the final doublet is placed upstream to cancel the sextupolar geometrical aberrations

Synchrotron radiation in the FD sets a lower limit to the achievable IP rms spot size [85, 86] that depends on the FFS optics parameters and the beam emittance. This effect drives the length of the FD quadrupoles for high energy colliders.

7.6.2 Final Focus Optimization

The transfer map between the start of the FFS and the IP is given by $x_{\mathrm{IP}} = X_{\mathrm{jklmn}}\ x^{\mathrm{j}}\ {p_x}^{\mathrm{k}}\ y^{\mathrm{l}}\ {p_y}^{\mathrm{m}}\ \delta^{\mathrm{n}}$, where X_{jklm} are the map coefficients that can be extracted from MAD-X [87] and PTC [88] and the sum over repeated indexes applies. The standard quadratic deviation of the particle distribution at the IP is expressed as a function of the $\mathrm{X_{jklm}}$ coefficients and the entry beam sigmas as given in [89]. This allows for a semi-analytical optimization of any lattice parameters (like the strength of non-linear elements) so as to minimize the IP beam size.

7.6.3 Final Focus tuning

The unavoidable misalignments and field errors of the different components of the FFS result in an emittance dilution at the IP. FFS tuning refers to the process of bringing the machine to nominal performance and to maintain it in the presence of dynamic errors. The initial set-up procedure involves steering the beam through the centre of critical apertures and magnetic elements with known higher-order fields. Pre-computed knobs use orbit bumps at the sextupoles to orthogonally control all the different IP particle distribution correlations. These knobs are iteratively scanned until the minimum IP beam size is reached. Finally either single magnets strengths or higher order knobs [90, 91] can be scanned to minimize the higher-order aberrations.

7.7 Low Emittance Generation

S. Guiducci · Y. Papaphilippou

The high luminosity of a linear collider depends strongly on the generation of ultra-low emittance high-intensity bunches, with remarkable stability. Conventional electron sources and positron production schemes provide beams with several orders of magnitude larger emittances, than the ones needed. The required cooling mechanism is generated by the natural synchrotron radiation damping of the beam when circulating in rings.

The requested performance of the damping rings (DRs) is driven by the collider's principal parameters, the upstream or downstream systems' requirements, and especially the main linac RF. The parameters driving the design of the ILC [92] and CLIC are shown in Table 7.6. The technological choice of super-conducting over copper main linac RF cavities, clearly diversifies the DR design, although a number of approaches and challenges remain common. In the one flavour of DRs as CLIC, the bunch trains are relatively short with even shorter bunch spacing and with a high repetition rate. The ILC bunch train is ~220 km long and needs to be compressed and stored in a 3.2 km-long ring. In order to achieve the high luminosity, the ILC is based on bunches with high bunch charge and small emittances, whereas CLIC targets small bunch charges with much lower emittances. Modern X-ray storage rings in operation or construction phase are rapidly approaching these regimes, targeting ultra-low transverse emittances. Especially for the vertical emittance, requiring challenging alignment tolerances and stringent control of the optics and orbit, X-ray rings in operation have approached the quantum limit of vertical emittance, i.e. values below 1 pm [93].

For CLIC, the large input emittance for the positron beam and the high repetition rate necessitates a two-stage beam damping, with a pre-damping ring [94]. For ILC, there is no pre-damping stage and the DRs need a large acceptance for the injected beams, especially for positrons.

Most of the design challenges of the DRs are driven by the extremely high bunch density and the associated collective effects. In this respect, the DR parameters (Table 7.7) are carefully chosen and optimised in order to mitigate these effects [95, 96].

Table 7.6 CLIC versus ILC parameters driving the DRs design

Parameters	ILC	CLIC
Bunch population (10^9)	20	4.1
Bunch spacing (ns)	554	0.5
Number of bunches/train	1312	312
Number of trains	1	1
Repetition rate (Hz)	5	50
Ex. H/V/L norm. emittances (μm, nm, keV m)	(5.5, 20, 33)	(0.5, 5, 6)

Table 7.7 ILC and CLIC DRs design parameters

Damping ring parameters	ILC	CLIC
Energy (GeV)	5.0	2.86
Circumference (m)	3.238	359.4
Energy loss/turn (MeV)	4.5	5.8
RF voltage (MV)	14	6.5
Compaction factor (10^{-4})	3.3	1.2
Damping time x/s (ms)	24/12	1.2/0.6
Number of arc cells/wigglers	150/54	90/40
Dipole/wiggler field (T)	0.23/2.2	0.69–2.3/3.5

In the case of CLIC, the steady state emittance is dominated by Intra-Beam Scattering (IBS). The ring energy [97] and lattice design [96], (racetrack shape with TME arc cells with variable field dipoles [98] and long straight sections filled with super-conducting wiggler [99] FODOs) is optimized for reducing IBS. The larger emittance specification of ILC, allows for higher ring energy, thus relaxing collective effects.

Due to the very small beam size especially in the vertical plane, IBS is large. In order to mitigate its value within manageable limits, the ring is made as compact as possible, and the longitudinal beam size has to be increased [10P2, 100].

The key systems to allow damping the beam to ultra-low horizontal emittance in a compact ring during the short time between two machine pulses like in CLIC are high-field super-conducting damping wigglers with short period. Prototypes have been built and tested in a synchrotron light source, including novel cooling concepts [101]. Higher field mock-ups based on Nb_3Sn technology are under development and tests [102].

The combination of high bunch density and short bunch spacing triggers two stream instabilities for both ILC and CLIC DRs. In the e^--ring, the fast ion instability can be avoided with low vacuum pressure, partial ring filling and bunch-by-bunch transverse feedback [103]. In order to mitigate the electron cloud build up and avoid the instability to occur in the e^+-ring, the secondary electron yield (SEY) of the vacuum chambers has to be limited to below 1.2–1.3 and the photo-emission yield (PEY) has to be very low, from a few down to 0.1% [104]. The low SEY can be achieved with chamber coatings, as TiN, NEG or amorphous carbon [105, 106], whereas the low PEY necessitates an efficient photon absorption scheme.

The e-cloud mitigation, low emittance generation, fast kicker technology and the associated diagnostics are studied in dedicated test facilities (CESR-TA, ATF), synchrotron light sources as well as at various laboratories around the world.

The very high peak and average current of CLIC presents a big challenge due to the transient beam loading, especially for a high frequency RF system. Concepts of RF design including low-level RF feedback have been developed extrapolated from the design of e^+/e^- ring colliders [107].

As the beam stability requirement is quite stringent and typically 10% of the beam size, tight jitter tolerances for the rings extraction kickers are imposed, down to a few10^{-4}. Especially for the bunch-by-bunch extraction scheme of ILC, the kicker rise time of a few ns, is extremely challenging. An ILC extraction experiment using a prototype strip-line kicker was carried out at KEK-ATF [108]. It achieved multi-bunch beam extraction with 5.6 ns bunch spacing. The angle jitter of a single bunch beam was reduced to 3.5×10^{-4}, using a double kicker system. For CLIC, a stripline with an ultra-stable inductive adder as power source is being currently tested at ALBA synchrotron [109].

7.8 Recirculated Linacs and Energy Recovery

S. A. Bogacz · G. A. Krafft

Linear accelerators provide superb beam quality as defined by the sources, but they are current-limited due to the high cost of their RF drive. Circular accelerators, by contrast, offer high average beam current and exhibit high electrical efficiency (and associated cost reductions) because of the limited required investment in RF power. However, effects such as quantum excitation (incoherent synchrotron radiation) or space charge limit their beam quality. On the other hand, rings typically only come to equilibrium after many hundreds or thousands of turns, which significantly degrades beam quality (emittance, momentum spread, etc.).

Recirculated Linear Accelerators (RLAs) have several advantages that support electron beam parameters outside of the scope of the traditional ring accelerators or linacs [110]. Synchrotron radiation effects, as in electron storage rings, do not limit beam emittances and pulse lengths emerging from an RLA. The beam is circulated only a modest number of times, so the impacts of the degrading effects are then limited, and the beam quality may be much higher than the equilibrium beam quality inherent for rings.

Going a step further, in the Energy-Recovered Linac (ERL), the full-energy beam is returned to the accelerating structure out of phase with respect to the accelerating field after being used (collides, produces synchrotron radiation, drives a specific reaction, etc.). The beam is decelerated, returning the RF power in the beam to the accelerating structure, making this RF power available to accelerate a subsequent beam. The resulting system retains the excellent beam quality of a conventional linac—and, because of the recovery of significant levels of RF power—can provide high average beam current at excellent electrical efficiency and lower associated cost. The ERL concept is quite attractive because it provides linac-quality/brightness beam at storage ring beam powers. With the advent of operational ERLs, it may be possible to push average currents to levels approaching the best lepton storage rings in existence as of 2019. Furthermore, the production of high beam power with reduced RF drive represents improved electrical efficiency, introducing ‘green technology’ with significant cost reductions. Energy recovery

also provides an additional environmental advantage, as the total stored energy in the system is deposited at very low (injection) energy, providing mitigation of serious environmental/safety issues. Finally, ERLs, like linacs, offer a flexible time structure, allowing operation with single bunches, CW bunch trains, and virtually every combination between these options. As in other linac-based systems, ERLs can easily manipulate various portions of phase space independently of other portions; they are fully six-dimensional systems, supporting transverse matching to desired spot sizes, longitudinal matching to desired bunch length/energy spread ratios (via transverse/longitudinal coupling), and any (or all) of horizontal/vertical transverse/longitudinal phase space exchanges.

Next-generation light source or collider applications requiring the following elements should generally be well-suited to deploying a recirculated and/or energy-recovered linac: CW or other high duty factor operation, high beam average current, low delivered beam energy spread, and low delivered beam emittance. CW beam acceleration with high accelerating gradients (>10–20 MV/m) generally requires deploying a multi-pass RLA consisting of superconducting accelerator structures. GeV-scale RLAs at 100 mA average current would ordinarily require at least 100 MW of installed RF power merely to accelerate the beam load. Beam energy recovery allows substantial reduction of the RF beam loading of the cavities.

In applying this idea with a back-to-front beam recirculation, as illustrated in Fig. 7.9, the beam recirculation path length is chosen to be an integral number of RF wavelengths, plus approximately one-half of the RF wavelength. Because the beam sees accelerating phase on the lower accelerating beam passes through the linac, after a phase shift of 180 degrees, energy is delivered back to the (S)RF cavities by higher beam passes, and transferred directly to the accelerating beams without the need for additional power from other RF sources [111]. To the extent that the average beam load from the accelerating passes completely cancels the beam load from the decelerating beam passes, there is no limit to the average current that may be accelerated due to RF source capacity. Because the beam transit time through the recirculated linac is much smaller than the radiation-induced emittance growth times in the bending arcs, the beam longitudinal and transverse emittances can be much smaller in energy-recovered linacs than in storage ring accelerators that operate at the same energy. It should be noted that energy recovery is also an important element in the design of high average current electrostatic accelerators.

Beam energy recovery was first proposed as a way to construct high-luminosity colliders for high energy physics [112]. Although never realized in this application, energy-recovered accelerators have been built as electron cooling drivers and high-power free-electron laser drivers [113–115].

Many proposed applications benefit from the advantages of energy-recovered linacs. For example, Cornell University is investigating the energy-recovered linac as an undulator driver yielding superior, high average brilliance X-ray sources as an upgrade to their conventional synchrotron light facility [116]. Similar programs exist at Argonne and Daresbury Laboratories [117], and in Japan [118, 119]. Brookhaven National Laboratory and CERN are investigating the use of high average current

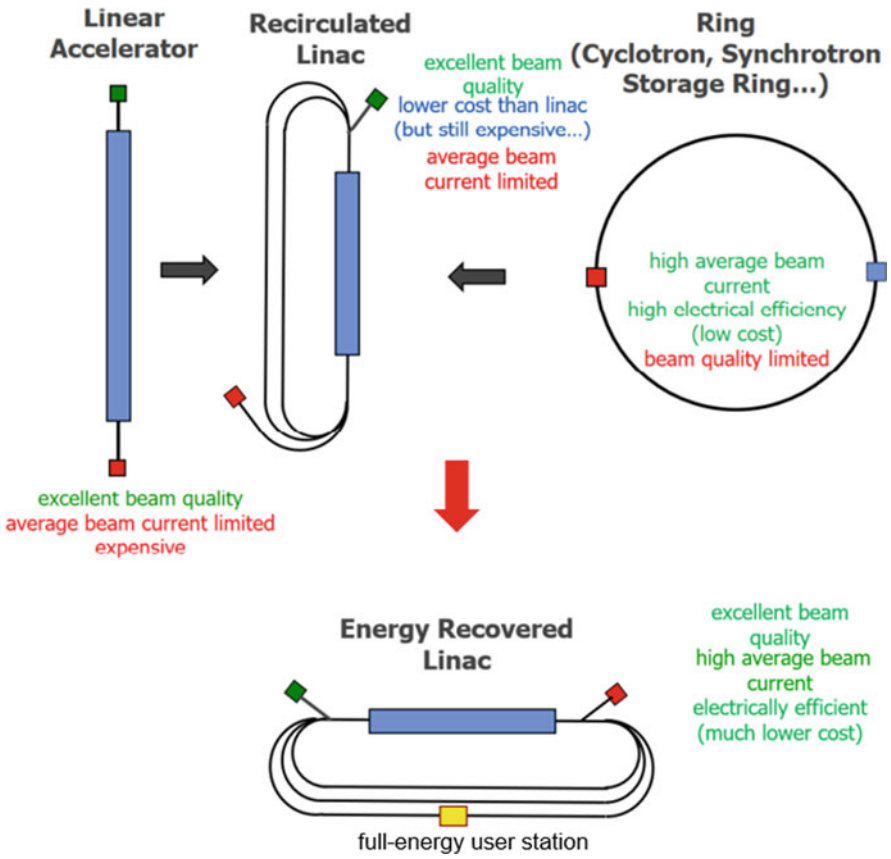

Fig. 7.9 Evolution of accelerator architectures driven by cost/performance optimization—the ERL architecture emerges as the final step—'the best of both worlds' (linacs, rings)

energy-recovery linacs as electron sources for high-luminosity electron-ion colliders [120]. Advanced RF-coolers have been proposed based on energy-recovered linacs.

Several important design issues for recirculated linacs are the high average current gun and injector, linac design, recirculating arc design, and beam stability. Historically, DC guns have been applied at recirculated and energy-recovered linacs, largely because they easily support CW beam. The desire to support higher beam quality in the injector has led to efforts to develop CW RF-based electron guns. Linac design philosophy has largely followed the example of the CEBAF accelerator where 'graded gradient' first-pass optics are designed to yield constant phase advance, and the higher beam passes are less focused because of the higher energy of higher beam passes. For a variety of reasons, superconducting recirculated linacs prior to 1990 used recirculation arcs that were isochronous, leading to FODO-type systems as in the large recirculation arcs of CEBAF, or the large energy acceptance design first deployed at Bates Laboratory [121, 122]. On the other hand, normal-

conducting devices have operated with non-isochronous recirculation and microtron phase stability [123] as an inherent design choice [124]. Recirculator optics based on two-bend and three-bend achromatic optics have been deployed. With the advent of beam energies where synchrotron radiation is an important part of the beam quality from the recirculator, arcs are being suitably designed and implemented to minimize emittance and energy spread growth, as at synchrotron radiation sources.

An additional multi-bunch beam instability potentially affects recirculated and energy-recovered linacs: multi-pass beam breakup (BBU) [125, 126]. In this instability, deflections of the beam generated by high order modes in the accelerating cavities can drive unstable feedback if the deflections translate after recirculation into position offsets that act to further excite the high order mode. This instability was first observed in the first superconducting recirculator at Illinois, and restricted the operating current in the early Stanford superconducting recirculator. When the much-larger-scale CEBAF accelerator was built, the solution to the instability problem was provided by building the linac from cavities that were known to have good HOM damping. This approach has continued to the present, where cavities have been designed and tested that are expected to support 100 mA to 1 A currents in recirculating linac arrangements.

Successful operations of high-power FEL drivers stimulated community interest in ERL technology, and there followed numerous proposals and a number of actual systems. These included: FEL drivers: the JLab IR Upgrade FEL [127], ALICE [128], and the JLab UV Demo FEL [129]; test facilities: CEBAF-ER [130], the KEK cERL [131], bERLinPro [132], ER@CEBAF [133], and PERLE [134, 135]; and systems associated with nuclear physics facilities: the BNL test ERL, an electron cooler concept [136], MESA [137], and most recently, conversion of the Darmstadt S-DALINAC to an ERL [138].

Having described the motivation for ERLs and how they operate, we briefly survey the contemporary ERL landscape, review progress to date, and detail challenges confronting upcoming generations of these machines. We also provide an overview of applications (servicing FELs, high-energy electron cooling systems, inverse Compton-driven gamma sources, internal-target experiments, accelerator science/technology test platforms).

7.8.1 Novosibirsk ERL

The Novosibirsk ERL—developed, built and commissioned at BINP in 2003—was the first multi-pass ERL operating in CW mode [139]. It initially reached a top energy of 12 MeV, with high average current of 30 mA [140]. The ERL is fed by a 300 kV electrostatic gun with a thermionic cathode ($Q \sim 1$ nC, $\tau = 1$ ns, $f_{rep} = 10$ kHz–50 MHz), followed by one bunching and two accelerating cavities for effective bunch compression. The facility uses a normal-conducting accelerating system at 180 MHz, with average power up to 0.5 kW (peak power of about 1 MW). The ERL drives three separate FELs (NovoFEL facility) [141] operating

in a spectral range of 90–240 microns. The ERL had recently (2015) been upgraded to 42 MeV, based on four-pass energy recovery to drive a short wave FELs in a spectral range of 8–15 microns [142].

7.8.2 S-DALINAC

The S-DALINAC energy-recovery linac is a superconducting electron accelerator operated at Technical University Darmstadt since 1991. The ERL was recently upgraded (2015–2016) and as of 2019 it is capable of operating as a one-pass, or two-pass ERL with maximum energies of approximately 34 or 68 MeV, respectively [143]. The ERL provides beam for Compton scattering of laser beams on intense electron beams to generate quasi-monochromatic, energy-tunable, fully polarized gamma-ray beams for photonuclear reactions [144]. The most recent upgrade [145] started in 2017, and would enable an increase of the maximum achievable energy close to its design value of 130 MeV. A newly-added beamline features a path-length adjustment system capable of changing the phase of the beam by a full RF cycle.

7.8.3 MESA

MESA is a recirculating superconducting accelerator under construction at Johannes Gutenberg-Universität Mainz. The facility [146] uses a superconducting accelerating system based on the TESLA operation frequency of 1.3 GHz. The 2-pass recirculating linac has been configured to operate in two different modes: the external beam (EB) mode, where a 150 μA polarized electron beam at 155 MeV is dumped after being used at the experiment, and in energy-recovery mode (ERL) with an unpolarized beam of 1 mA at 105 MeV [147]. At an upcoming later construction stage, MESA's maximum achievable beam current (in the ERL-mode) will be upgraded to 10 mA (unpolarized).

7.8.4 Compact ERL

The compact ERL (cERL) at KEK is a test accelerator to develop ERL technologies for high average beam current operation with high-quality beam performance [148]. The cERL consists of a photoinjector, a main linac for energy recovery, a recirculation loop, and a beam dump. To achieve energy-recovery operation with high average beam current, collimator tuning to reduce unwanted beam loss has been very important. After fine beam tuning and collimator tuning, stable CW operation with 0.9 mA average beam current was achieved. Upgrade efforts are under way to increase CW beam current to 10 mA through improved instrumentation. The

ERL transports a short electron bunch with a high repetition frequency of 1.3 GHz. Coherent, high-intensity THz radiation from such short electron bunches has many unique applications in material science.

7.8.5 bERLinPro

As of 2019, the Helmholtz-Zentrum Berlin is constructing the Energy-Recovery Linac Prototype bERLinPro, an SRF-based demonstration facility for the science and technology of ERLs for future high power, high brilliance electron beam applications [149]. bERLinPro is designed to accelerate a high current (100 mA, 50 MeV), high brilliance (normalized emittances below 1 mm·mrad) CW electron beam. The ERL as a prototype to demonstrate low normalized beam emittance of 1 mm·mrad at 100 mA and short pulses of about 2 ps. The high-brilliance beam will originate from a gun configured with (1.4 λ)/2 cell SRF cavity with a normal-conducting, high quantum efficiency. This injector is planned to support 6 mA beam current and up to 3.5 MeV beam kinetic energy.

7.8.6 CBETA

Cornell-BNL-ERL-Test-Accelerator (CBETA) is a test ERL [150], featuring four accelerating passes through the superconducting linac with a single Fixed Field Alternating Linear Gradient (FFA-LG) return beamline built of the Halbach-type permanent magnets. The CBETA ERL accelerates electrons from 42 to 150 MeV, with a 6 MeV injector. The novelty is that four electron beams, with energies of 42, 78, 114, and 150 MeV, are merged by spreader beamlines into single-arc FFA-LG beamlines. The electron beams from the main linac cryomodule pass through the FFA-LG arc and are adiabatically merged into a single straight line. This is the first 4-pass superconducting ERL and the first single permanent magnet return line. It promises to deliver unprecedentedly high beam current with simultaneously small emittance. A collaboration between Cornell and Brookhaven National Laboratory has constructed the CBETA facility on the Cornell campus [151], and commissioning is ongoing as of the summer of 2019. A DC photo-emitter electron source, a high-power SRF injector linac, a high-current SRF linac for energy recovery, and a permanent-magnet return loop have been assembled to the 4-turn SRF ERL. CBETA provides essential R&D for the EIC. Furthermore, the high-brightness beam with 150 MeV and up to 40 mA will have applications beyond EIC cooling and basic accelerator research, for industry, nuclear physics, and X-ray science.

7.8.7 PERLE

PERLE (Powerful ERL for Experiments) is a novel ERL test facility [152] which has been designed to validate choices for a 60 GeV ERL foreseen in the design of the LHeC [153] and the FCC-eh. Its main thrust is to probe high current, CW, multi-pass operation with superconducting cavities at 802 MHz (and perhaps other frequencies of interest). With very high transient beam power (~10 MW), PERLE offers an opportunity for controllable studies of every beam dynamic effect of interest in the next generation of ERL design; PERLE will become a 'stepping stone' between present state-of-the-art 1 MW ERLs and future 100 MW scale applications. PERLE design features a flexible momentum compaction lattice architecture in six vertically stacked return arcs, and a high-current, 5 MeV photo-injector. With only one pair of four-cavity cryomodules, 400 MeV beam energy will be reached in three recirculation passes, with beam currents of appoximately 20 mA. The beam will be decelerated in three consecutive passes back to the injection energy. Work on the engineering design of PERLE has just begun as of summer 2019.

In summary, the next-generation ERLs under study or in construction in 2019 take performance to the next (10 MW) level, and include bERLinPro, CBETA, and PERLE. These systems will provide the experience and knowledge base for fourth-generation objective systems such as electron-ion collider electron coolers, XFEL drivers, and high-energy colliders.

A more detailed comparison of present and next-generation systems is given in Table 7.8 [154]. Certain characteristics of the next generation are apparent: not only do projected beam powers climb by an order of magnitude as noted, but the number of passes, the power multiplier, and the dynamic range all increase, and both accelerated and recovered beams are transported in shared beamlines. All of these features are natural evolutionary consequences of system design optimization in the pursuit of higher performance with a lower cost.

Table 7.8 Comparison of selected present and future generation ERLs

	JLab ERLs	S-DALINAC	bERLinPro	CBETA	PERLE
Gun technology	DC	Thermionic	SRF	DC	DC
Total # passes	2	2	2	8	6
Recirculation architecture	Conventional	Conventional	Conventional	FFG	Conventional
Acceleration/recovery multipass transport	Linac only	Linac only	Linac only	Common	Common
RF frequency (GHz)	1.5	3	1.3	1.3	0.8
Nominal bunch charge (pC)	135	Very low	77	77	320
Design current (mA)	10	Very low	100	40	20
Total current in linac (mA)	9.1	Very low	200	320	120
Energy (GeV)	0.165	~0.0425	~0.05	~0.15	0.5–1
Beam power (MW)	1.25 ($>>P_{RF}$)	Low ($<P_{RF}$)	10 ($>>P_{RF}$)	6 ($>>P_{RF}$)	10–20 ($>>P_{RF}$)
Energy at dump (MeV)	11	2.5	5	5	5
E_{full}/E_{dump}	15–20	17	10	30	100–200

References

1. D. Proch: *Quest for high gradient*, Proc. CERN Accelerator School, Superconductivity in Particle Accelerators, H. Rissen (ed.), CERN 96-03 (1996) 201.
2. W. Weingarten: *Superconducting cavities – Basics*, Proc. CERN Accelerator School, Superconductivity in Particle Accelerators, H. Rissen (ed.), CERN 96-03 (1996) 167.
3. R. Hardekopf, et al: Particle Accelerator Conf. (1999) 3597.
4. T. Raubenheimer, et al: Particle Accelerator Conf. (2007) 1944.
5. R. Brinkmann: Linear Accelerator Conf. (2008) 5.
6. H. Ao: *Status of J-PARC Linac Energy Upgrade*, Linear Accelerator Conf. (2010).
7. J. Delahaye, et al: Intern. Particle Accelerator Conf. (2010) 4769.
8. T. Sugimura, et al: Intern. Particle Accelerator Conf. (2010) 4290.
9. J.-Y. Raguin, et al: Linac Conf. (2012) 501.
10. T. Raubenheimer, et al: FEL Conf. (2015) 618.
11. F. Loehl, et al: Linac Conf. (2016) 22.
12. G. Loew: Handbook of Accelerator Physics and Engineering, World Scientific (1999) 26.
13. J. Potter: Handbook of Accelerator Physics and Engineering, World Scientific (1999) 513.
14. I. Bazarov: Particle Accelerator Conf. (2005) 382.
15. J. Simpson: Handbook of Accelerator Physics and Engineering, World Scientific (1999) 46.
16. B. O'Shea et al: Nature Comm. (2016) 7:12763.
17. B. Blue et al: Phys. Rev. Let. (2003) 90-21-214801-1.
18. M. Hogan, et al: Particle Accelerator Conf. (2007) 1910.
19. S. Gessner, et al: Nature Comm. 7 (2016) 11785.
20. C. Joshi, et al: Plasma Phys. Control Fusion (2018) 1.
21. A. Gonsalves, et al: Particle Accelerator Conf. (2007) 1911.
22. W. Leemans, et al: Phys. Rev. Let. 113 (2014) 245002.
23. E. Colby, et al: Particle Accelerator Conf. (2007) 3115.
24. J. England et al: Rev. Mod. Phys. (2014) 1337.
25. R. Hollebeek: Nucl. Instrum. Meth. 184 (1981) 33.
26. P. Chen, K. Yokoya: Phys. Rev. D 38 (1988a) 987.
27. R.J. Noble: Nucl. Instrum. Meth. A 256 (1987) 427.
28. M. Bell, J.S. Bell: Part. Accel. 24 (1988) 1.
29. R. Blankenbecler, S.D. Drell: Phys. Rev. Lett. 61 (1988) 2324.
30. P. Chen, K. Yokoya: Phys. Rev. Lett. 61 (1988b) 1101.
31. M. Jacob, T.T. Wu: Nucl. Phys. B 303 (1988) 389.
32. V.N. Baier, V.M. Katkov, V.M. Strakhovenko: Nucl. Phys. B 328 (1989) 387.
33. For CAIN see: P. Chen, et al.: CAIN: Conglomérat d'ABEL et d'Interactions Nonlinéaires, Nucl. Instrum. Meth. A 355 (1995) 107.
34. For GUINEA-PIG see: D. Schulte*: Electro-magnetic and hadronic background in the interaction region of the TESLA collider* (PhD thesis), DESY-TESLA-97-08 (1996).
35. For GUINEA-PIG++ see: D. Schulte, et al.: *GUINEA-PIG++ : An Upgraded Version of the Linear Collider Beam Beam Interaction Simulation Code GUINEA-PIG*, PAC07-THPMN010.
36. D. Schulte, *Beam-beam effects in linear colliders,* in CERN-2017-006-SP (CERN, Geneva, 2017).
37. P. Chen, V. Telnov: Phys. Rev. Lett. 63 (1990) 1976.
38. ILC WEB: http://www.linearcollider.org
39. ILC TDR: http://www.linearcollider.org/ILC/Publications/Technical-Design-Report
40. ILC 250 GeV: https://arxiv.org/abs/1711.00568
41. CLIC WEB: http://clic.cern
42. CLIC CDR: http://clic-study.web.cern.ch/content/conceptual-design-report
43. CLIC 380 GeV: https://arxiv.org/abs/1608.07537
44. LHC cost: http://cds.cern.ch/record/2255762/file

45. E-XFEL: http://accelconf.web.cern.ch/AccelConf/ipac2017/papers/moxaa1.pdf and https://www.xfel.eu/
46. LCLS II: http://accelconf.web.cern.ch/AccelConf/ipac2017/papers/tupab130.pdf and https://lcls.slac.stanford.edu/lcls-ii
47. SCRF R&D: A. Grassellino et al., "Unprecedented quality factors at accelerating gradients up to 45 MV/m in niobium superconducting resonators via low temperature nitrogen infusion", Supercond. Sci. Technol. 30 (2017) 094004 (https://doi.org/10.1088/1361-6668/aa7afe)
48. ILC Japan 2012: http://www.jahep.org/office/doc/201202_hecsubc_report.pdf
49. CTF3 results: http://accelconf.web.cern.ch/AccelConf/ipac2017/papers/tuzb1.pdf
50. X-band applications: http://cerncourier.com/cws/article/cern/52358
51. CESRTA results: http://accelconf.web.cern.ch/AccelConf/IPAC10/papers/tuymh02.pdf
52. FACET studies: Latina, Andrea et al., "Experimental demonstration of a global dispersion-free steering correction at the new linac test facility at SLAC", Physical Review Special Topics - Accelerators and Beams. 17. 042803 (https://doi.org/10.1103/PhysRevSTAB.17.042803) (2014)
53. ATF2 results: https://agenda.linearcollider.org/event/7014/contributions/36882/attachments/30069/44951/ATF2_okugi_20160601.pdf
54. R.B. Neal, et al., The Stanford two-miles linear accelerator, New York: W.A. Benjamin, 1968.
55. E. Jensen, CTF3 Drive Beam accelerating structures, Proc. LINAC2002, 2002, Gyeongju, Korea, CERN/PS 2002-068(RF), and CLIC note 538
56. A. Grudiev, W. Wuensch, DESIGN OF THE CLIC MAIN LINAC ACCELERATING STRUCTURE FOR CLIC CONCEPTUAL DESIGN REPORT, Proceedings of Linear Accelerator Conference LINAC2010, Tsukuba, Japan, 2010.
57. H. Padamsee: *RF superconductivity*, Wiley-VCH Verlag (2009).
58. H. Padamsee, J. Knobloch, Tom Hays: *RF superconductivity for accelerators*, John Wiley & Sons Inc. (1998).
59. H. Padamsee: *Designing superconducting cavities for accelerators*, Proc. CERN Accelerator School, S. Russenschuck, G. Vandoni (eds.), CERN-2004-008, (2004).
60. J. Sekutowicz: *Design of a low loss SRF cavity for the ILC*, PAC'05, Knoxville, (2005) 3342.
61. R. Geng: *Review for new shapes for high gradients*, Physica C 441 (2006) 145.
62. FLASH/TESLA facility project: http://flash.desy.de/tesla/tesla_documentation/
63. European XFEL project: http://www.xfel.eu/
64. ILC project: http://www.linearcollider.org/
65. A. Yamamoto: *Global R&D effort for the ILC LINAC technology*, Proc. EPAC-08, MOYBGM01, Genova, (2008).
66. L. Evans, S. Michizono, and A. Yamamoto: *International Linear Collider (ILC) – Overview* "KASOKUKI", Journal of Particle Accelerator Society of Japan, **14**, No. 4 (2017) 194-200.
67. A. Yamamoto: *Superconducting RF Cavity Development for the International Linear Collider*, IEEE Trans. Appl. Superconductivity. **19** (3) (2009) 1387-1393.
68. A. Yamamoto and K. Yokoya: *Linear Colliders*, Review of Accelerator Science and Technology, Vol. 7 (2014) 1-22.
69. K.L.F. Bane, A. Mosnier, A. Novokhatsky, K. Yokoya: *Calculation of the Short-Range longitudinal wakeelds in the NLC linac*, in: Proc. ICAP 1998, Monterey, CA, November 1998.
70. A.W. Chao: Physics of Collective Beam Instabilities in High Energy Accelerators, Wiley-Interscience, 1st edition, January 1993.
71. Th.P. Wangler: RF Linear Accelerators. Wiley-VCH, 2nd edition, March 2008.
72. M.G. Minty, F. Zimmermann: Measurement and Control of Charged Particle Beams, Springer, 1st edition, August 2003.
73. A.W. Chao: Handbook of Accelerator Physics and Engineering, Second Edition, World Scientific Publ., 2013.
74. V. Balakin, et al.: Phys. Rev. Lett. 74 (1995) 2479-2482.
75. M.S. Zisman: *The PEP-II Project*, LBL-34556 CBP Note-036.
76. E. Kikutani, et al.: *KEKB Accelerator Papers*, KEK Preprint 2001-157, December 2001.

77. P. Raimondi, A. Seryi: Phys. Rev. Lett. 86 (2001) 3779-3782.
78. P. Bambade, et al. (ATF Collaboration): Phys. Rev. ST Accel. Beams 13 (2010) 042801.
79. G.R. White et al.: Phys. Rev. Lett. 112, 034802 (2014).
80. E. Marin, et al.: Phys. Rev. ST Accel. Beams 17, 021002 (2014)
81. M. Patecki, et al.: Phys. Rev. Accel. Beams 19, 101001 (2016).
82. R. Brinkmann, Report No. DESYM-90-14, 1990.
83. H. Garcia Morales and R. Tomas Garcia: Phys. Rev. ST Accel. Beams, 17, 101001 (2014).
84. A. Seryi et al.: *A recipe for linear collider final focus system design,* PAC 2003.
85. K. Oide: Phys. Rev. Lett. 61, 1713 (1988).
86. O. R. Blanco, et al.: Phys. Rev. Accel. Beams 19, 021002 (2016).
87. http://mad.web.cern.ch/mad/
88. E. Forest, F. Schmidt, E. McIntosh: KEK Report 2002–3.
89. R. Tomas: Phys. Rev. ST Accel. Beams 9, 081001 (2006).
90. N.J. Walker, J. Irwin, M. Woodley: *Global tuning knobs for the SLC final focus*, PAC 93, and *Third-Order Corrections to the SLC Final Focus*, SLAC-PUB 6206, May 1993
91. T. Okugi et al.: Phys. Rev. ST. Accel. Beams 17, 023501 (2014).
92. Adolphsen, C., et al. (eds.): "The International Linear Collider Technical Design Report - Vol. 3 – Accelerator Baseline Design, (2013), arXiv: 1306.6328 [physics.acc-ph] ILC-REPORT-2013-040.
93. Low Emittance Rings workshop series, 2010, 2011, 2013, 2014, 2015, 2016, 2018.
94. Antoniou, F. and Papaphilippou, Y.: "Analytical considerations for linear and nonlinear optimization of TME cells. Application to the CLIC pre-damping rings", Phys. Rev. ST Accel. Beams 17, 064002, 2014.
95. Guiducci, S., et al.: " 10G1 Updates to the International Linear Collider Damping Rings Baseline Design", (2011), Proceedings of IPAC2011, San Sebastián, Spain
96. Papadopoulou, S., Papaphilippou, Y., Antoniou, F.: "Emittance reduction with variable bending magnet strengths: Analytical optics considerations", Phys. Rev. ST Accel. Beams, submitted, 2018.
97. Papaphilippou, Y, et al.: "Parameter scan for the CLIC damping rings", EPAC'08, Genova, 2008.
98. Dominguez Martinez, M. A., et al.: "Design of a dipole with longitudinally variable field using permanent magnets for CLIC damping rings", IEEE Trans. on Applied Superconductivity 28, 3, 2018.
99. Schoerling, D., et al.: "Design and System Integration of the Superconducting Wiggler Magnets for the CLIC Damping Rings", Phys. Rev. ST Accel. Beams 15, 042401, 2012.
100. Antoniou, F., Optics design of Intrabeam Scattering dominated damping rings, Ph.D. thesis, National Technical University of Athens, 2013.
101. Bernhard, A., et al.: "A CLIC Damping Wiggler Prototype at ANKA: Commissioning and Preparations for a Beam Dynamics Experimental Program", IPAC'16, Busan, 2016.
102. Garcia Fajardo, L., et al.: "A CLIC Damping Wiggler Prototype at ANKA: Commissioning and Preparations for a Beam Dynamics Experimental Program", Proceedings, 24th International Conference on Magnet Technology (MT-24): Seoul, Korea, October 18-23, 2015, IEEE Trans. Appl. Supercond. 26, 4100506, 2016.
103. Kim, E.-S., Ohmi, K.: "Simulations on the Fast-Ion Instability in the International Linear Collider Damping Rings", Jpn. J. Appl. Phys. 48 (2009) 086501.
104. Rumolo, G., et al.: "Electron Cloud Build Up and Instability in the CLIC Damping Rings", EPAC'08, Genova, 2008.
105. Shaposhnikova, E., et al.: "Experimental studies of carbon coatings as possible means of suppressing beam induced electron multi-pacting in the CERN SPS", PAC'09, Vancouver, 2009.
106. Palmer M., et al.: "Electron Cloud at Low Emittance in CesrTA", IPAC'10, Kyoto, 2010.
107. Grudiev, A.: "Conceptual Design of the CLIC Damping Ring RF System", TUPPR026, Proceedings of IPAC2012, New Orleans, Louisiana, USA, 1870-1872, 2012.

108. Naito, T., et al.: "Multi-bunch Beam Extraction by using Strip-line Kicker at KEK-ATF", IPAC'10, Kyoto, 2010.
109. Belver-Aguilar, C., et al.: "The Stripline Kicker Prototype for the CLIC Damping Rings at ALBA: Installation, Commissioning and Beam Characterisation", IPAC'18, Vancouver, 2018.
110. L. Merminga, D.R. Douglas and G.A. Krafft, 'High-Current Energy-Recovering Electron Linacs', Ann. Rev. Nuc. Part. Sci., 53, 387-429 (2003)
111. T. Smith *et al.*, "Development of the SCA/FEL for Use In Biomedical and Materials Science Experiments", NIM-A, **259**, 26-30 (1987).
112. M. Tigner, 'A Possible Apparatus for Electron Clashing-Beam Experiments', Nuovo Cimento, **37**, 1228 (1965)
113. G.R. Neil *et al.*, 'Sustained Kilowatt Lasing in a Free-Electron Laser with Same-Cell Energy Recovery', Phys. Rev. Lett. 84, 662-665 24 January 2000a
114. R. Hajima, *et al.*,' Optics and beam transport in energy-recovery linacs', *Nucl. Instr. and Meth. A***507** 115 (2003)
115. E.J. Minehara *et al.*, 'JAERI superconducting RF linac-based free-electron laser-facility', NIM-A, **445** pp. 183-186 (2000)
116. S.M. Gruner, *et al.*, *Review of Scientific Instruments***73**, p. 1402 (2002)
117. S. Saveliev, *et al.*, *Proc. IPAC2010*, p. 2350, 2010
118. K. Umemori, *et al.*, *Proc. SRF-2009*, p. 896, 2009
119. T. Sakanaka, *et al*., *Proc. IPAC2010,* p. 2338, 2010
120. V.N. Litvinenko, *Proc. IPAC2010,* p. 2364, 2010
121. J. Flanz, S. Kowalski and C. Sargent, IEEE Trans. Nucl. Sci. **NS-28** 2847 (1981)
122. J. Flanz, *Proc. 1989 Particle Accelerator Conference* p. 1349 (1989)
123. V.I. Veksler, *Proc. USSR Acad. Sci.***43** (1944) 346; *J. Phys. USSR***9** 153 (1945)
124. H. Herminghaus, *et al.*, *IEEE Trans. Nucl. Sci.***NS-30** 3274 (1983)
125. R.E. Rand, '*Recirculating Electron Accelerators'*, Harwood Academic Publishing, (1984)
126. G.A. Krafft and J.J. Bisognano, *Proc. 1987 Part. Acc. Conf.* p. 1356 (1987)
127. G.R. Neil *et al.*, 'Sustained Kilowatt Lasing in a Free-Electron Laser with Same-Cell Energy Recovery' Phys. Rev. Lett. 84, 662-665 24 (2000b)
128. F. Jackson *et al.*, 'The Status of the ALICE R&D Facility at STFC Daresbury Laboratory', Proc. IPAC2011, TUODA03, pp. 934-936, 2011
129. R. Legg *et al.*, 'Operation and Commissioning of the Jefferson Lab UV FEL Using an SRF Driver ERL', Proc. IPAC2011, THP172, pp. 2432-2434, 2011
130. S.A. Bogacz *et al*., 'CEBAF Energy Recovery Experiment', Proc. PAC 2003, IEEE, pp 195, (2003)
131. T. Kasuga, 'Future Light Source Based On Energy Recovery Linac in Japan', Proc. APAC 2007, TUPMA046, pp. 172-174, 2007
132. J. Knobloch *et al.*, 'Status of the bERLinPro Energy Recovery Project', Proc. IPAC2012, MOPPP015, pp. 601-603, 2012
133. F. Méot et al., 'ER@CEBAF - A High Energy, Multi-pass Energy Recovery Experiment at CEBAF', Proc. of IPAC2016, TUOBA02, 2016
134. D Angal-Kalinin *et al*., 'PERLE. Powerful Energy Recovery Linac for Experiments. Conceptual Design Report', J. Phys. G: Nucl. Part. Phys. **45** 065003 (2018)
135. S. A. Bogacz *et al.*, 'PERLE - Lattice Design and Beam Dynamics Studies', Proc. IPAC2018, THPMK105, 2018
136. V. Litvinenko *et al.*, 'High Current Energy Recovery Linac at BNL', Proc. PAC2005, RPPT032, pp. 2242-2244, 2005
137. K. Aulenbacher, 'The MESA accelerator', *Workshop to Explore Physics with Intense, Polarized Electron Beams at 50-300 MEV*, R. Milner *et al.*, ed., AIP Conf. Proc. 1563 (2013)
138. M. Arnold *et al.*, 'ERL Mode of S-DALINAC: Design and Status', Proc. ERL 2017, CERN (2017a)
139. N. A. Vinokurov *et al*., Preprint BINP, (1978) 78-88; Proc. of the 6th Soviet Union Accelerator Conference, VII (1978) 233-236

140. N.G Gavrilov *et al*., 'Project of CW Racetrack Microtron-Recuperator for Free-Electron Lasers' Nucl. Instr. and Meth. A304 (1991) 228-229
141. G. N. Kulipanov *et al*., 'Novosibirsk Free-Electron Laser – Facility Description and Recent Experiments', IEEE Trans. on Terahertz Science and Technology, 5(5) (2015) 798–809
142. Y.V. Getmanov *et al*., 'Full spatial coherent multi-turn ERL x-ray source (MARS) based on two Linacs', Bristol: IOP Publishing – Journal of Physics: Conference Series, (2013) 4
143. N. Pietralla, Nuclear Physics News, Vol. 28, No. 2, (2018) 4
144. C. Kremer *et al*., Phys. Rev. Lett. 117, 172503 (2016)
145. M. Arnold *et al*., 'Construction of a Third Recirculation for the S-DALINAC' *Proc. LINAC 2016*, pp. 168-170, 2017b
146. D. Simon, K. Aulenbacher, R. Heine and F. Schlander, 'Lattice and beam dynamics of the energy recovery mode of the Mainz energy recovering superconducting accelerator MESA' *Proc. IPAC2015*, 2015
147. F. Hug, K. Aulenbacher, R. Heine, B. Ledroit and D. Simon, 'MESA - an ERL project for particle physics experiments' *Proc. LINAC2016*, 2016
148. N. Nakamura *et al*., 'Present Status of the Compact ERL at KEK' *Proc. of IPAC2014, MOPRO110*, 2014
149. M. Abo-Bakr *et al*., 'Status Report of the Berlin Energy Recovery Linac Project BERLinPro' *Proc. IPAC2018,* THPMF034, 2018
150. R.J. Michnoff *et al*., 'CBETA – Novel Superconducting ERL' *Proc. IPAC2019*, TUPGW102, 2019
151. C. Gulliford *et al*., 'CBETA Beam Commissioning Results' *Proc. IPAC2019,* MOPRB076, 2019
152. G. Arduini *et al*., 'PERLE: Powerful ERL for Experiments - Conceptual Design Report' accepted for publication in Journal of Physics G (2017)
153. D. Pellegrini, A. Latina, D. Schulte and S.A. Bogacz, 'Beam-dynamics Driven Design of the LHeC Energy Recovery Linac', PRST-AB, **18**, 121004 (2015)
154. D. Douglas, C. Tennant, S. Benson and S.A. Bogacz, 'Why PERLE? – Historical Context and Technological Motivation', JLAB-TN-18-014 (2018)